

# Politecnico di Torino

MASTER'S DEGREE IN BIOMEDICAL ENGINEERING



MASTER'S DEGREE THESIS

## Experimental setup for SAR and temperature focusing in microwave cancer hyperthermia

**Advisor:**

Prof. Giuseppe Vecchi

**Candidate:**

Alberto Bottino

**Co-advisors:**

Dott. Rossella Gaffoglio

Dott. Giorgio Giordanengo

Dott. Marcello Zucchi

**Academic Year 2020/2021**

# Contents

<b>Introduction</b>	<b>1</b>
<b>1 Hyperthermia cancer therapy</b>	<b>3</b>
1.1 Thermal therapies: overview . . . . .	3
1.2 Hyperthermia: state of the art . . . . .	4
1.3 Governing equations . . . . .	6
1.3.1 Maxwell's equations . . . . .	7
1.3.2 Bioheat equation . . . . .	10
1.3.3 Specific Absorption Rate . . . . .	12
1.4 Hyperthermia applicators . . . . .	13
1.4.1 Patch antennas . . . . .	13
1.4.2 Scattering parameters . . . . .	16
<b>2 Simulation analysis</b>	<b>18</b>
2.1 COMSOL Multiphysics . . . . .	18
2.2 Numerical model . . . . .	20
2.3 S-parameters . . . . .	23
2.4 SAR-based focusing . . . . .	25
2.4.1 Particle Swarm Optimization . . . . .	27
<b>3 Experimental setup</b>	<b>29</b>
3.1 Electronic components . . . . .	31
3.2 S-parameters characterization . . . . .	38
3.3 Radiofrequency electromagnetic field exposure guidelines . . . . .	40
3.4 Temperature measurement setup . . . . .	42
3.4.1 Fiber Bragg Gratings . . . . .	43
3.4.2 Thermal imaging camera . . . . .	45
<b>4 Heating session results</b>	<b>47</b>
4.1 SAR focusing in COMSOL Multiphysics . . . . .	47
4.2 Temperature maps . . . . .	48

4.2.1	Temperature maps comparison . . . . .	50
4.3	Thermal characterization . . . . .	53
4.4	Dielectric characterization: error analysis . . . . .	55
4.4.1	Marsland and Evans method . . . . .	56
4.4.2	Error analysis . . . . .	58
<b>5</b>	<b>Conclusions</b>	<b>61</b>
	Bibliography . . . . .	63

## Abstract

Microwave cancer hyperthermia is a thermal therapy used in cancer treatments, which consists in heating the tumor region to a temperature of 40–44 °C by exposure to non-ionizing microwave radiation.

In particular, it has been demonstrated that combining hyperthermia with chemotherapy and/or radiotherapy (i.e., two of the pillars of today's cancer treatment) provides a better clinical outcome than chemotherapy or radiotherapy alone (enhances drugs absorption and sensitizes tissues to radiations). However, to ensure a successful therapy, it is important to focus the heating exclusively on the tumor, avoiding the formation of hotspots in the surrounding healthy tissues. For the treatment of internal tumors (such as head and neck tumors), this is currently achieved by optimizing the feedings of phased array applicators.

The following thesis describes the implementation of an experimental apparatus for hyperthermia treatments in the neck region, from the preparation of the electronic setup and optimization of the array feedings to the temperature measurements on a cylindrical agar-based phantom mimicking the muscle tissue.

In particular, this thesis reports: (1) the analysis and fine-tuning of numerical models reproducing the experimental apparatus; (2) a study of the algorithms employed to focus the specific absorption rate (SAR) on a precise region inside the muscle phantom; (3) the experimental measurements concerning the setup of the electronic components; (4) the characterization of each antenna of the array (calculation of the scattering parameters); (5) both thermal and dielectric characterization of the agar-based phantom; (6) a preliminary assessment of the experimental setup (e.g., positioning of temperature sensors, electromagnetic compatibility measurements of the system) and finally, (7) heating of the system, temperature acquisitions and comparison with simulations.

# Introduction

In the last two decades, studies on hyperthermia have continuously increased. The main reason for this interest is the potential role of hyperthermia in cancer treatment: it has been demonstrated that combining hyperthermia with radiotherapy and/or chemotherapy results in the same clinical outcome with a lower dose (of drug or ionizing radiation) than radiotherapy or chemotherapy alone [1]. Moreover, microwave hyperthermia treatment is carried out using non-ionizing radiation, so no further toxicity is added to the cancer treatment: this is an important aspect as many studies on cancer treatment aim to achieve the same clinical outcome with reduced toxicity and side effects [2]. However, since the effectiveness of hyperthermia depends on the thermal dose [3], microwaves must be properly combined to obtain an optimal focusing on the tumor region.

The present thesis describes the experimental setup of a mock-up reproducing a system for hyperthermia treatment in the neck region. The main parts of this demonstrator are: the phantom mimicking human neck, the electronic components, the phased array applicator with patch antennas and the temperature sensors.

In particular, the study was conducted by means of both numerical simulations and experimental measurements followed by the analysis and comparison of the obtained data. Therefore, the project includes:

- an experimental part, in which an agar-based phantom of the neck region is selectively heated by a circular array of 8 patch antennas;
- a simulation part, managed with COMSOL Multiphysics<sup>®</sup>, in which the same phantom is numerically modelled and both SAR and temperature maps are computed;
- data analysis, to elaborate both experimental and simulation data in order to verify that the focusing algorithm correctly works and approximately gives the same results in both cases.

Although the simulation and experimental parts were carried out in parallel, they will be presented in two different chapters for sake of clarity.

In particular, this thesis is structured as follows:

*Chapter 1:* after a brief overview on thermal therapies (differing in temperature, duration and biological effect), the state of the art of hyperthermia treatment is presented, with a specific mention to the HYPERcollar 3D applicator [4]. Another section, with respective subsections, is dedicated to the governing equations needed to describe the problem, while the last one is about hyperthermia applicators (patch antennas) and scattering parameters (S-parameters).

*Chapter 2:* this chapter is dedicated to the simulation part of the thesis, so it describes the software (COMSOL Multiphysics<sup>®</sup>) used to create the numerical model (described as well in a separate section).

In the last two sections, a study on the frequency dependence of S-parameters and the Particle Swarm Optimization (PSO) algorithm used for SAR focusing are reported.

*Chapter 3:* this chapter reports a description of the experimental apparatus, including the electronic components (e.g., circulators, phase shifters, directional couplers etc.) and the comparison between the S-parameters experimentally evaluated and those obtained with COMSOL Multiphysics. Moreover, the results of the electromagnetic compatibility measurements conducted for safety reasons are reported. Finally, the temperature measurement setup, including fiber-optic sensors and a thermal camera, is described.

*Chapter 4:* SAR and temperature maps resulting from the optimization algorithm are shown. In particular, a comparison between simulation and experimental results is conducted; in addition, thermal characterization results are presented. Finally, an error analysis on the dielectric parameters (permittivity and electrical conductivity) of the agar-based mixture evaluated with two different methods is carried out.

*Chapter 5:* Comments on the results, critical aspects and possible future developments are presented.

# Chapter 1

## Hyperthermia cancer therapy

The hyperthermia treatment is a thermal therapy in which the temperature of the tumor is increased up to 40–44 °C. In microwave hyperthermia the target is heated by non-ionizing electromagnetic radiation: in particular, for the treatment of internal tumors, the feedings of a circular antenna array are optimized to create constructive interference exclusively in the tumor region.

### 1.1 Thermal therapies: overview

Thermal therapies have always played an important role in healthcare (Roman baths are one of the most famous examples of the use of heat for therapeutic purposes). In general, the aim of thermal therapies is to achieve the best clinical outcome with no damage to healthy tissues [5].

The capability to bring and maintain temperature at certain levels (above or below 0 °C) results in various applications, ranging from cryoablation to the treatment of rheumatic diseases, from hyperthermia to thermal surgery.

There are several thermal therapies that differ in working temperature, treatment duration and, consequently, biological effect achieved. These include:

- thermal ablation: brings tissue temperature above 60 °C (inactivation zone) for 5–15 minutes. The main damages are protein denaturation and membrane rupture; the tissue, once inactivated, is digested by macrophages. Similar effects can be obtained through cryoablation (working temperature of approximately -75 °C);
- diathermy: mainly applied in physiotherapy, it uses temperatures up to 41 °C for 5 to 20 minutes in several sessions;
- hyperthermia: working temperatures (40–44 °C) lower than thermal ablation but for longer periods of time (almost 60 minutes).

The biological effect (i.e., improvement in the effectiveness of radiotherapy and/or chemotherapy) occurs after several sessions.

The working temperatures and therapy duration given above do not represent clear-cut divisions between thermal therapies, but provide an idea of the parameters used to achieve a certain biological effect.

Although the working temperatures of thermal therapies are slightly different in the literature, the range of 40–44 °C defined for hyperthermia at ESHO 2018<sup>1</sup> is widely accepted [6].

## 1.2 Hyperthermia: state of the art

To increase the temperature of the target, non-ionizing electromagnetic radiation is used (frequencies of 434 MHz, 915 MHz or 2450 MHz are the most common in hyperthermia treatments [5]): this heating method presents the important advantage of not adding further toxicity to tumor treatments. In addition, combining hyperthermia with chemotherapy and radiotherapy provides better clinical outcomes than radiotherapy or chemotherapy alone, limiting the side effects on the surrounding healthy tissues [7, 8].

The reason of these effects is that if the temperature of a biological tissue changes, its properties also change, becoming more sensitive to cancer therapy [1]. For example, as reported in literature [9, 10], comparing clinical outcomes achieved using chemotherapy alone or combined with hyperthermia, it has been demonstrated that in the second case the therapy is more effective at the same dose.

Hyperthermia also leads to radio-sensitivity enhancement [11, 12]: tumor cells absorb more ionizing radiation during thermoradiotherapy treatments (i.e., radiotherapy combined with hyperthermia), while healthy cells better tolerate the radiation: this allows “to expand” the therapeutic window, and thus limiting toxicity to healthy tissues.

One of the main critical points of this therapy is to focus the temperature increase on a specific part of the body (where the tumor is located) limiting the formation of hotspots (i.e., high temperature in surrounding healthy tissues): in order to find the correct input parameters which ensure an optimal focusing, treatment planning is a fundamental step [1]. So, an hyperthermia treatment is not only limited to tissue heating, but there is an important preparation part that consists in: (1) acquisition of CT or MRI images and

---

<sup>1</sup>32nd Annual Meeting of the European Society for Hyperthermic Oncology, Berlin, Germany, May 16–19, 2018.

creation of 3D patient model; (2) thermal and electromagnetic characterization of tissues; (3) treatment planning (e.g., properly selection of antenna phases and amplitudes, CT scan for the catheter locations).

Another important aspect of hyperthermia treatments is to have a constant control of the temperature during the thermal therapy to guarantee both the treatment efficacy (it has been demonstrated that the clinical outcome depends on the thermal dose<sup>2</sup> [13,14]) and the safety of patients. Furthermore, considering that in biological systems even a small variation of 1 °C or 2 °C can lead to different situations, and being the number of invasive temperature sensors limited (for patient's comfort), it becomes important to predict the temperature distribution.

To monitor in real time the effects of electromagnetic treatments, VEDO (the Visualisation Tool for Electromagnetic Dosimetry and Optimisation) has been developed [15]: based on patient feedback (pain complaints) and threshold values not to be exceeded, this software tool helps hyperthermia treatment planning (HTP) for deep head and neck (H&N) tumors.

During hyperthermia treatment in the H&N region the so-called waterbolus is positioned around the neck of the patient (Figure 1.1). The waterbolus is a doughnut-shaped bag filled with circulating demineralized water at a constant temperature of about 20–25 °C, having the dual function to couple the electromagnetic field into the patient and to control the skin surface temperature, avoiding superficial hotspots.

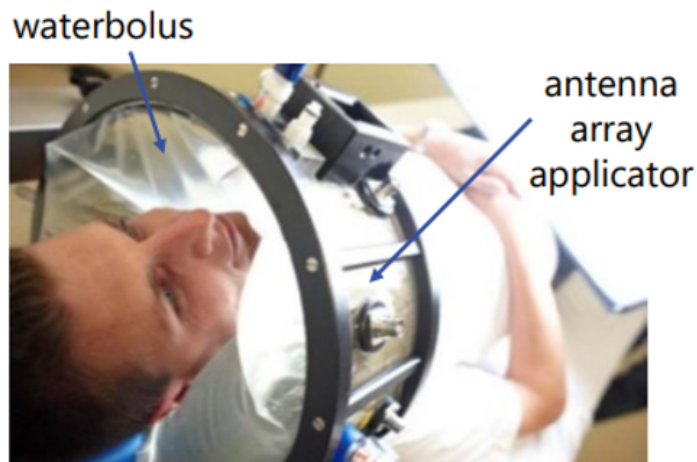


Figure 1.1: HYPERcollar for H&N tumor treatments [16].

---

<sup>2</sup>The thermal dose means the working temperature and the duration of a thermal treatment to achieve a specific effect.

In hyperthermia treatment planning (HTP) the selection of a proper applicator is crucial to achieve a good focusing in most patients: for example, Paulides et al. [4] have developed the HYPERcollar, a novel applicator for hyperthermia treatment of head and neck (H&N) tumors made up of two circular arrays of 6 antennas operating at 434 MHz (Figure 1.1).

The feedings (phases and amplitudes) of these antennas have to be properly optimized; in particular, there are two main methods to optimize antenna feedings: by optimizing the Specific Absorption Rate (SAR) in the tumor or by directly maximizing the temperature in that target region. The first method (used in this thesis) requires less numerical cost than the second, which however is less affected by the uncertainty characterizing thermal tissue parameters, and can lead to satisfying temperature focusing by applying additional temperature-based refinement techniques, as described in [17].

### 1.3 Governing equations

Thanks to its various advantages, electromagnetic heating is one of the main technique for hyperthermia treatment. First of all, it is a non-invasive technique, so it does not present the risks that an invasive one does (and, in general, patients prefer non-invasive techniques). In addition, in the frequency range of interest ( $10^8$  Hz –  $10^{10}$  Hz), the radiation is non-ionizing, so there are no health hazards. A further advantage is that electromagnetic heating, differently from other heating processes like convection, is almost instantaneous and uniform [18].

Microwaves present also some limits, such as the complicated management of surrounding tissues (greater difficulties in focusing on the tumor due to the large wavelength): for this reason, a focusing technique using the particle swarm optimization (PSO) algorithm was implemented to maximize the SAR in the target (tumor tissue) and to minimize it in the other tissues. In particular, relative phases and amplitudes of the antennas are optimized to obtain an optimal focusing on the target, while the overall power level of the array can be increased to reach higher temperatures.

To give an overview of what happens during a hyperthermia treatment, both Maxwell's equations and Pennes bioheat equation are necessary: the former describes the external source (i.e., the microwaves), the latter the heat exchange in biological tissues.

### 1.3.1 Maxwell's equations

Electromagnetic waves are the results of oscillating magnetic and electric fields in space and time.

The spectrum of electromagnetic waves (Figure 1.2) can be divided in two main groups: ionizing radiation and non-ionizing radiation (including microwaves). For hyperthermia treatments non-ionizing radiations are used: in particular, in the examined case, the working frequency of 434 MHz lies in the microwaves range.

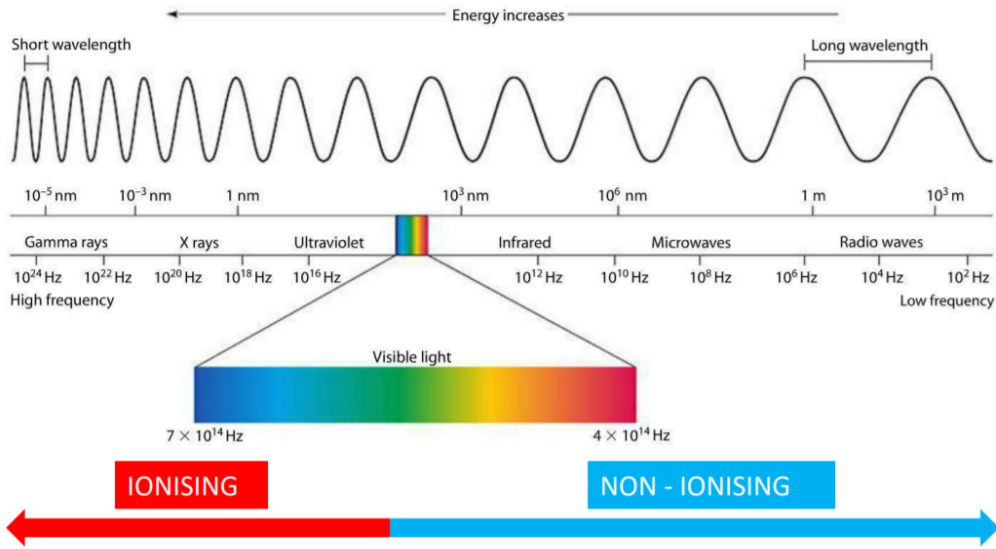


Figure 1.2: Electromagnetic spectrum [19].

The four vectorized Maxwell's equations in vacuum (reformulated in the following form by O.Heaviside [20]) are:

$$\nabla \cdot \mathbf{E} = \frac{\rho}{\epsilon_0}, \quad (1.1)$$

$$\nabla \cdot \mathbf{H} = 0, \quad (1.2)$$

$$-\nabla \times \mathbf{E} = \frac{\partial}{\partial t} \mu_0 \mathbf{H}, \quad (1.3)$$

$$\nabla \times \mathbf{H} = \frac{\partial}{\partial t} \epsilon_0 \mathbf{E} + \mathbf{J}. \quad (1.4)$$

Rewriting (1.3) and (1.4) with time-harmonic representation, we obtain:

$$-\nabla \times \mathbf{E} = j\omega\mu_0\mathbf{H} , \quad (1.5)$$

$$\nabla \times \mathbf{H} = j\omega\epsilon_0\mathbf{E} + \mathbf{J} , \quad (1.6)$$

in which the vacuum dielectric permittivity ( $\epsilon_0 = 8.85 \cdot 10^{-12}$  F/m) and vacuum magnetic permeability ( $\mu_0 = 4\pi \cdot 10^{-7}$  H/m) are two natural constants,  $\omega = 2\pi f$  ( $f$  is the frequency, Hz),  $\mathbf{E}$  (V/m) and  $\mathbf{H}$  (A/m) are the electric and magnetic field vectors respectively, and  $\mathbf{J}$  (A/m<sup>2</sup>) is the electric current density, equal to  $\mathbf{J} = \sigma\mathbf{E}$  (where  $\sigma$  is the frequency-dependent electrical conductivity which encompasses all of the dissipation phenomena related to mass transport).

The charges in the matter when exposed to an electromagnetic field can act in two different ways: as free charges or as bound charges. In the first case, the effect is the conduction, so the charges are free to move in the conductive mean (drift current). In the other case, the dipoles (neutral molecules with zero total charge lacking of a symmetric distribution of the electrons) are subjected to a mechanical effect that is not translational (as in the conductive case), but rotational. So, although their total charge is zero, the dipoles start to rotate and to align with the external field, influencing it: this contribution must be added to the external electric field.

Both polarization and conduction phenomena, in the absence of an intense magnetic field, depend only on the electric field: in general, conduction could also be generated by a magnetic field, but in lot of materials, such as biological tissues, charges move only because of the electric field<sup>3</sup>.

The equation solved in COMSOL Multiphysics combines equations (1.5) and (1.6) by introducing the dielectric and magnetic properties of the materials involved (muscle tissue in the case presented in this thesis):

$$\frac{1}{\mu_r} \nabla \times (\nabla \times \mathbf{E}) - k_0^2 \left( \epsilon_r - \frac{j\sigma}{\omega\epsilon_0} \right) \mathbf{E} = 0 , \quad (1.7)$$

---

<sup>3</sup>It can be demonstrated (by substituting the Lorentz force  $\mathbf{F} = q\mathbf{E} + q\mathbf{v} \times \mathbf{B}$  into the general work expression  $W = \mathbf{F} \cdot \Delta s$ ) that the magnetic field does not work on charges: it neither adds nor subtracts energy. This does not mean that the magnetic field is irrelevant to the energy effects and can be neglected: in dynamic conditions, electric and magnetic fields are linked by Maxwell's equations, so, although the magnetic field has no direct effect, it influences the electric field, which instead works on the charges.

where:

- $\epsilon_r$  is the relative permittivity of the considered material, which, for muscle tissue, is approximately 59 at  $f = 434$  MHz [21];
- $\sigma$  is the electrical conductivity, approximately equal to 0.86 S/m for muscle tissue at  $f = 434$  MHz [21];
- $\mu_r$  is the relative permeability, set equal to 1 (as stated at page 8, biological tissues are materials with low magnetic reactivity);
- $k_0$  ( $\text{m}^{-1}$ ) is the wavenumber in the vacuum, equal to:  $k_0 = \omega\sqrt{\epsilon_0\mu_0}$ .

In (1.7), the medium is considered homogeneous, so its dielectric properties ( $\epsilon_r$ ,  $\sigma$ ,  $\mu_r$ ) are assumed constants in space.

The relative permittivity and the electrical conductivity of the medium in which the electromagnetic waves propagate (i.e., the agar-based mixture mimicking neck muscle), strongly influence the resulting temperature and SAR maps: for this reason, the dielectric characterization of the medium represents an important step.

Many studies, leading to many models, have been carried out on the frequency dependence of both permittivity and conductivity (this dependence is called dispersion phenomenon). Among these models, one of the most widely used is the Debye model [22], an empirical model valid in the case of a homogeneous medium which well-describes the dielectric relaxation of almost all means. A more accurate model was provided by the Cole brothers (Cole-Cole model [23]), who introduced an empirical exponent in the Debye model.

In biological tissues two dissipation phenomena occur: those due to conductivity (resistive losses) and those due to dipole oscillations (dielectric losses). In general, a collective permittivity ( $\tilde{\epsilon} = \epsilon_r - j\frac{\sigma}{\omega\epsilon_0}$ ) that encompasses both dissipation phenomena is defined.

The equations describing electromagnetic field behaviour in the matter are essentially the same as in the vacuum case, with the difference of complex  $\tilde{\epsilon}$  (obtained from experimental measurements) rather than  $\epsilon_0$ .

It is important to specify that since the dielectric values used to build the models are derived from ex vivo measurements of explant healthy tissues, they represent a source of uncertainty.

### 1.3.2 Bioheat equation

Biological heating evaluation starts from the analysis of the electromagnetic power dissipation averaged over time scales characteristic of thermal phenomena.

In particular, to find the resulting temperature variation, Pennes' bioheat equation [24] is applied:

$$\rho C \frac{\partial T}{\partial t} = \nabla \cdot (k \nabla T) + q_s . \quad (1.8)$$

In (1.8), which is only valid for time scales longer than average thermal ones (few tens of minutes),  $q_s$  is the source term. If  $q_s$  is equal to 0, the temperature variation is only related to thermal gradients  $\nabla \cdot (k \nabla T)$ .

In particular, the source term can be written as  $q_s = q_{hs} + q_{bp} + q_m$ , where:

- $q_{hs}$  is the heat source term (the electromagnetic heating in the considered case);
- $q_m$  is the metabolic heat generation term, i.e., the heat generated by metabolic reactions;
- $q_{bp}$  is the heat related to blood perfusion (blood also acts as a thermo-regulating liquid).

The other variables in equation (1.8) are the mass density  $\rho$  ( $\text{kg}/\text{m}^3$ ) and specific heat capacity  $C$  ( $\text{J}/(\text{kg} \cdot ^\circ\text{C})$ ) of the considered tissue, while  $k$  ( $\text{W}/(\text{m} \cdot ^\circ\text{C})$ ) is its thermal conductivity.

The blood perfusion term is proportional to the temperature difference between the temperature in a specific region and the temperature in a "quiet zone" (i.e., the arterial temperature, which can be considered constant).

So, the blood perfusion can be evaluated as:

$$q_{bp} = -\rho_b C_b \omega_b (T - T_a) . \quad (1.9)$$

In (1.9),  $\rho_b$  and  $C_b$  are the mass density and the specific heat of the blood, respectively, while  $T_a$  is the arterial temperature and  $\omega_b$  is the perfusion rate (i.e., the number of times in the time unit that blood in the control volume is completely recycled).

Perfusion rate, which can also be normalized to the tissue mass of the considered district, is difficult to be estimated: the values found are almost always indirect measures which vary with temperature (an important approximation will be to consider the parameters as temperature-independent).

The minus sign in (1.9) represents what the blood does: to compensate temperature variations, if the temperature increases, it takes away the heat, if the temperature decreases, it carries the heat in.

There are two main particular cases in which, starting from (1.8), temperature variation can be easily evaluated: initial transient and stationary state. In both cases, two simplifying assumptions are included in the model: (1) the metabolic heat generation is considered negligible, so  $q_m \approx 0$  and (2) the applied electromagnetic field is assumed to be uniform.

In the initial transient (the first minutes), the effects of blood thermoregulation can be neglected, so  $q_{bp} \approx 0$ . Under these conditions, the relation between SAR and temperature variation in the initial transient can be found as:

$$\Delta T|_{initial} \approx \frac{\text{SAR}}{C} \cdot \Delta t, \quad (1.10)$$

so, in the initial transient, the temperature variation  $\Delta T$  is proportional to the SAR, which is a measure of the electromagnetic energy related to the tissue.

In the other case (the stationary state), the variation in temperature over time is negligible, so  $\frac{\partial T_{ss}}{\partial t} \approx 0$  and the simplified bioheat equation in this case becomes  $-q_{bp} = q_{em} + \nabla \cdot (k \nabla T_{ss})$ , where  $T_{ss}$  is the temperature reached in the stationary state (when the thermal gradient is negligible) and  $q_{em}$ , as will be shown in Subsection 1.3.3, is equal to  $q_{em} = \frac{1}{2} \sigma \mathbf{E}^2$ .

Assuming that the electromagnetic source term dominates the thermal gradient term, so  $q_{em} \gg |\nabla \cdot (k \nabla T_{ss})|$ , the equation becomes:

$$q_{em} = \rho_b C_b \omega_b (T_{ss} - T_a), \quad (1.11)$$

which, by substituting the expression  $q_{em} = \frac{1}{2} \sigma \mathbf{E}^2$ , can be written as:

$$\frac{1}{2} \sigma \mathbf{E}^2 = \rho_b C_b \omega_b (T_{ss} - T_a). \quad (1.12)$$

Therefore, as much heat is generated by the electromagnetic field, as is carried away by the heat flux associated with blood thermoregulation.

### 1.3.3 Specific Absorption Rate

The electromagnetic field carries a certain amount of energy that is perceptible only as it interacts with matter (this interaction depends on the ratio between the dimension of the object and the wavelength).

Considering a volume  $\Omega$  in which the electromagnetic field propagates, the energy balance is:

$$p_{diss,\Omega}(t) + \frac{d}{dt}W_{\Omega}(t) = p_{\partial\Omega}(t) , \quad (1.13)$$

in which:

- $p_{diss,\Omega}(t)$  is the power dissipated in the volume: this energy changes only its nature, from ordered to disordered;
- $W_{\Omega}(t)$  is the stored energy in  $\Omega$ ;
- $p_{\partial\Omega}(t)$  is the energy transport through the surface.

The power dissipation term is equal to:

$$\frac{p_{diss}(t)}{d\Omega} = \mathbf{E} \cdot \sigma \mathbf{E} = \sigma |\mathbf{E}(t)|^2 , \quad (1.14)$$

which is equal, in the harmonic form, to  $\frac{\sigma}{2}|\mathbf{E}|^2$ . This term corresponds to the heat source: the power dissipation resulting in the change from ordered energy to heat warms tissues (important aspect for both therapeutic and safety aspects).

In particular, the Specific Absorption Rate (SAR) is defined as:

$$\text{SAR} = \frac{\sigma}{2\rho} |\mathbf{E}|^2 , \quad (1.15)$$

where  $\rho$  (kg/m<sup>3</sup>) and  $\sigma$  (S/m) are the mass density and the electrical conductivity of the considered tissue, respectively, while  $|\mathbf{E}|$  (V/m) is the electric field's magnitude (peak value).

Some considerations concerning the SAR are:

- it is a quantity related to small volumes: the mass density  $\rho$  does not changes very much in the volume, but the conductivity  $\sigma$  does;
- it varies with the square of the electric field, so it is a highly variable measurement. For this reason, SAR is averaged over a volume: if the electric field is almost homogeneous in the considered volume, the averaged SAR does not differ too much from the local SAR;

- the unit of measurement is W/kg, so it is the absorbed power per unit mass;
- SAR definition (1.15) does not include the blood perfusion.

SAR is used to measure electromagnetic field strength in its interaction with biological systems: on one hand, it can be used to evaluate the potential damages that electromagnetic waves can generate (for example, SAR is used for the regulation of some electronic devices); on the other hand, SAR can be used to plan a thermal therapy: starting from the SAR distribution map and solving the bioheat equation, the corresponding temperature map is obtained.

Although SAR represents the external heat source, it is important to point out that the obtained biological effects are related to the thermal dose [3] (so, to temperature and time exposure), not to the SAR.

## 1.4 Hyperthermia applicators

Depending on tumor location, different applicators can be selected. In particular, for superficial tumors, single antennas are usually used [25], whereas for internal tumors (such as many in the head and neck region), arrays of antennas should be used (as in this thesis). It has been demonstrated that, for sub-superficial tumors treatment, phased-array applicators leads to a better target coverage than the single planar applicator [26].

### 1.4.1 Patch antennas

The IEEE Standard Definitions of Terms for Antennas (IEEE Std 145–1983) [27] defines the antenna as “*a means for radiating or receiving radio waves.*” In the considered case, the antenna has been used as a device for transmitting energy in the form of electromagnetic waves.

Depending on the application and purpose, there are different types of antenna: in the studied case a patch antenna has been employed.

Patch (or microstrip) antennas are made up of a thin metallic layer (patch) deposited on a grounded substrate of thickness  $h_{sub}$  and relative permittivity  $\epsilon_r$  (Figure 1.3).

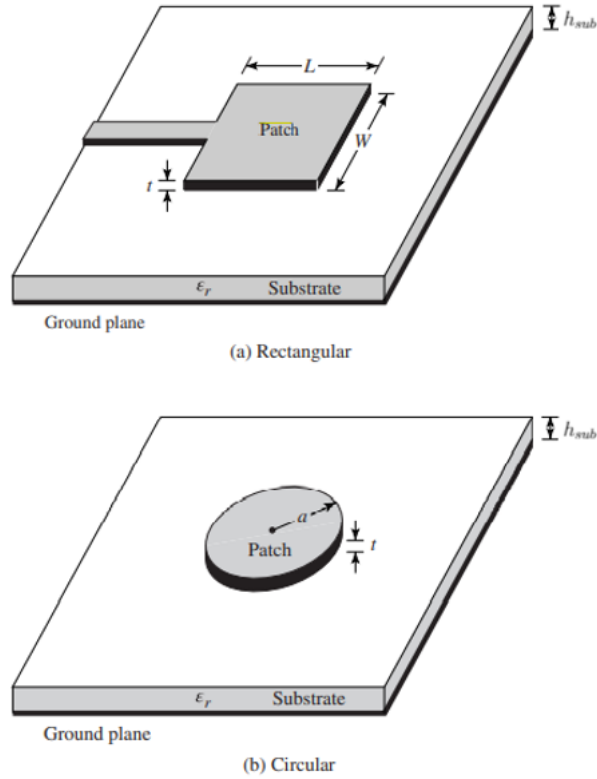


Figure 1.3: Representation of a rectangular (upper row) and circular (lower row) patch antenna [28].

Rectangular and circular metallic patch are the most used shapes: in particular, for our purposes, a rectangular shape of width  $W$  and length  $L$  (both measured in mm) has been considered. These two parameters ( $W$  and  $L$ ),  $x_f$  (i.e., coaxial pin distance from the edge of the patch) and the distance  $h_{sub}$  between the ground and the patch are the parameters to be optimized during the antenna design in order to improve the performance (i.e., lower reflection coefficient) of the antenna at a frequency of 434 MHz.

In particular, the antenna optimization was carried out in the electromagnetic simulation software CST Microwave Studio<sup>®</sup> by considering a single antenna in a simplified environment (a water domain with a muscle layer in front of the single antenna) to reduce the computational time and the complexity of the problem (Figure 1.4).

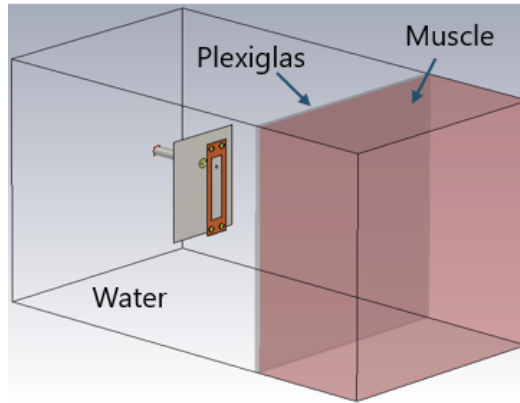


Figure 1.4: Antenna modelled in a simplified environment.

The considered antenna is: (1) composed by a water background (as it is designed to work immersed in water of the waterbolus), (2) designed (for construction reasons) on a thin layer of I-Tera dielectric on which ground and patch are printed and (3) fed by Teflon-coated coaxial cable.

The optimization is performed to minimize the reflection coefficient  $S_{11}$  at 434 MHz (Subsection 1.4.2) with sufficiently wide bandwidth around this frequency: as shown in Figure 1.5, the achieved  $S_{11}$  curve presents a bandwidth (-15 dB) of 20 MHz around the central value  $f = 434$  MHz.

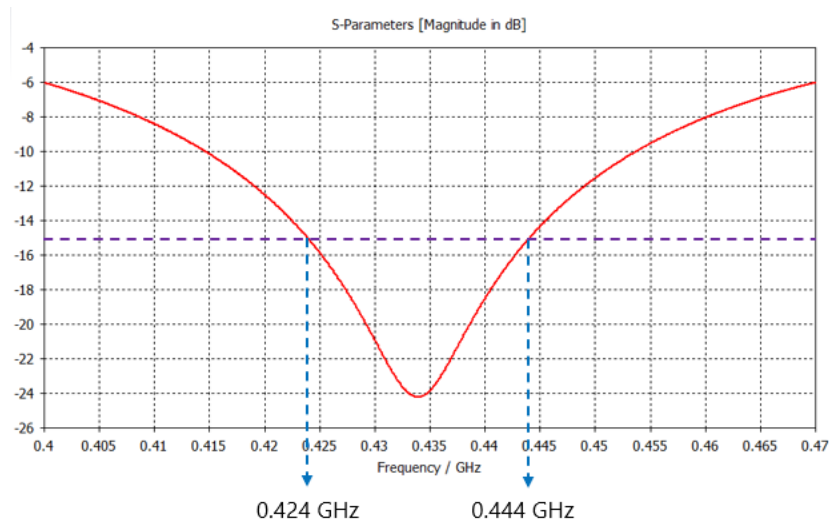


Figure 1.5: Antenna optimized to have the minimum  $S_{11}$  at 434 MHz with a sufficiently wide bandwidth.

The optimized geometric parameters are reported in Table 1.1.

$W$ (mm)	$L$	$h_{sub}$ (mm)	$x_f$ (mm)
33.85	7.13	10.50	5.66

Table 1.1: Optimized microstrip parameters obtained in CST.

It should be specified that the value of  $h_{sub} = 10.50$  mm differs from the one obtained through the simulations. The reason for this difference is linked to the presence of water near the coaxial pin: the water enters through the small hole of the pin and forms a sort of layer above the Teflon dielectric (which is not exactly in contact with the I-Tera substrate), leading to a resonance shift. For this reason, the patch-ground distance has been properly tuned manually.

### 1.4.2 Scattering parameters

The Scattering parameters (also called S-parameters), are complex numbers (with a specific amplitude and phase) which describe the behaviour of a network (a set of one or more ports) as a function of frequency. In particular, each port (in the considered case, each patch antenna) can pass, absorb and/or reflect RF energy.

Considering 2 antennas (port 1, the input, and port 2, the output), four parameters can be evaluated:

1.  $S_{11}$  is the input reflection coefficient and represents the power reflected from the input antenna (port 1). It is equal to the ratio between the amplitude of the reflected signal to that of the incident signal at port 1.
2.  $S_{12}$  (and  $S_{21}$ ) are the transmission coefficients, which represent the gain or the loss between input and output. In general, the parameter  $S_{xy}$  represents the response at port  $y$  due to a signal at port  $x$ .
3.  $S_{22}$ , the output reflection coefficient, indicates the power reflected from the output antenna (port 2). It is equal to the ratio between the amplitude of the reflected signal and that of the incident signal at port 2.

All the S-parameters are grouped in a NxN square matrix, the S-matrix, where N is the number of ports: since the considered array is composed by 8 antennas, the resulting S-matrix is 8x8.

Along the diagonal of this square matrix there are the reflection coefficients, while the elements outside the diagonal refer to the transmission coefficients.

S-parameters depend also from the impedance: ideally, if the impedance of the source matches the load, all the forward power is transferred to the load [29]. However, in the real case, the source impedance does not match the load and this causes part of the forward power to be reflected back to the source. In particular, since the impedance varies with the frequency, the portion of reflected power depends on the frequency: for this reason it is important to measure the power that is actually emitted by each antenna by measuring the S-parameters (in particular, if the optimization concerns a single antenna, as in the previous subsection, the reflection coefficient  $S_{11}$  is considered).

When all antennas are switched on, it is possible to evaluate active S-parameters for the  $i$ -th antenna ( $S_i^a$ ) as:

$$S_i^a = \sum_{k=1}^{N_T} S_{ik} \frac{a_k^{exc}}{a_i^{exc}}, \quad (1.16)$$

where  $N_T = 8$  is the number of antennas and  $a^{exc}$  are the excitation coefficients given in input to each antenna.

The active S-parameters are one of the two outputs (beside the SAR distribution) that are evaluated in the phase optimization algorithm (Section 2.4).

# Chapter 2

## Simulation analysis

Numerical simulation represents an innovative tool for replicating a problem by creation of a model that reproduces the real world. Simulations are useful for predicting the system's behaviour or testing it under different conditions (e.g., high temperature or high pressure), making explicit the physical laws that govern a particular phenomenon. Different outputs and graphical representations can be obtained by changing the input data (e.g., material properties, boundary conditions or geometry), promoting comparisons and supporting decision making.

### 2.1 COMSOL Multiphysics

COMSOL Multiphysics<sup>®</sup> is a mathematical modeling software developed by COMSOL for modelling and solving multiphysics problems.

“Multiphysics” means that it deals with different physics domains (such as electrical, mechanical, thermal, chemical etc.) that can be combined by the user according to the problem to reproduce.

As reported in the COMSOL official website [30], creating and solving a numerical simulation follows a single standard workflow:

1. Setting up the model: the user chooses space dimension and physics of the problem, i.e., the equations involved. In the considered case, Maxwell's equations (electromagnetic wave module in the frequency domain) and the bioheat transfer equation have been selected.
2. Creation of the geometry: different geometries and sizes can be set in order to reproduce the real system.

3. Materials properties definition: a specific type of material (with its properties) is assigned to each of the previously-defined geometric element. In particular, it is possible to select the material from a default list or to create a new one by defining its properties.
4. Setting of physics boundary conditions.
5. Creation of the mesh (meshing action means the discretization of the model in little elements, called mesh elements).
6. Running the simulation.
7. Post-processing results (several graphs and maps can be obtained).

Finite Element Method (FEM) [31] is applied in COMSOL Multiphysics to perform the simulations and solving the equations involved. FEM is a numerical method which converts a system of differential equations (with the proper boundary conditions) into a linear system of equations easier to solve, leading to an approximate solution. In particular, the complex geometry (Figure 2.1, left) is first meshed (Figure 2.1, right) and the boundary conditions assigned; then, the equations are set for each mesh element, resulting in a system of algebraic equations. The solution of the entire problem is thus reduced to a global system of simple equations that model the finite elements (mesh elements).

It is important to note that each mesh element contains all the material and structural properties assigned from the user.

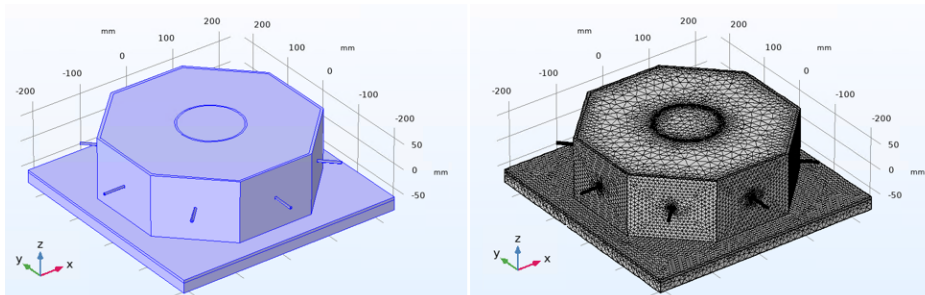


Figure 2.1: Meshing action: the prototype model (left) is subdivided into discrete elements (right) for which the linear system of equations is assembled.

Mesh elements can have different shapes and dimensions: the bigger are the elements, the faster meshing action and the simulation will be, but the solution will be less precise; similarly, finer mesh elements require more time

to solve the problem (so, it is possible that the amount of computational power needed would be too much), but more accurate results are obtained. Therefore, solution accuracy depends on mesh settings: too fine mesh elements could present almost the same results (the equations solved in neighbouring mesh elements lead to the same results as the boundary conditions will be very similar); on the contrary, with a very big mesh element, it is not possible to see what happens inside each block, so less precise results will be obtained. For this reason, mesh element (type and size) has to be adapted to the considered physics (in general COMSOL Multiphysics does it automatically).

## 2.2 Numerical model

Since hyperthermia's efficacy is strictly related to the quality of the heating process, a precise and accurate simulation of SAR and temperature distributions in the target and in the surrounding healthy tissues is necessary. Hence, numerical simulations have been performed in COMSOL Multiphysics (in particular, COMSOL Multiphysics 5.6 has been used for this thesis [30]) to solve Maxwell's equation (1.7) and Pennes equation (1.8) in a model properly built to reproduce the experimental prototype.

The COMSOL model, built following the standard steps illustrated on page 19, consists in 3 Plexiglas cylinders (mimicking the neck, the trachea and the spinal cord) and a sphere with a diameter of 25 mm, representing the target in which SAR must be focused, surrounded by a circular array of 8 patch antennas immersed in a water domain (mimicking the waterbolus)(Figure 2.2).

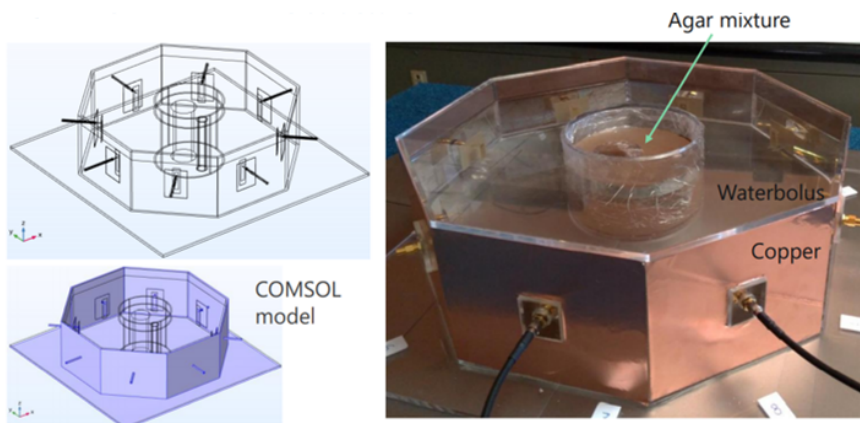


Figure 2.2: COMSOL model (left) reproducing the experimental prototype (right) with the circular array made of 8 patch antennas.

To reduce the computational burden required by a sufficiently fine mesh (and, so, to save time during every simulation run) the coaxial cable feeding each patch antenna is simulated replacing the external metal coating and the inner wire with infinitely thin surfaces with a Perfect Electric Conductor (PEC) condition defined on them. This allowed to remove the internal domain inside the inner wires, reducing the number of mesh elements (and, therefore, the time) needed to simulate the model.

The base of the Plexiglas prototype lays on microwaves absorbing foams and a metal table (simulated imposing a PEC condition). Moreover, between the Plexiglas base of the prototype and the foam absorbers, a layer of magnetic absorbers is placed and simulated by a Transition Boundary Condition (TBC).

In particular, dielectric parameters of magnetic absorbers are selected considering both datasheet values and the ones measured through a SPEAG probe [32](Figure 2.3).

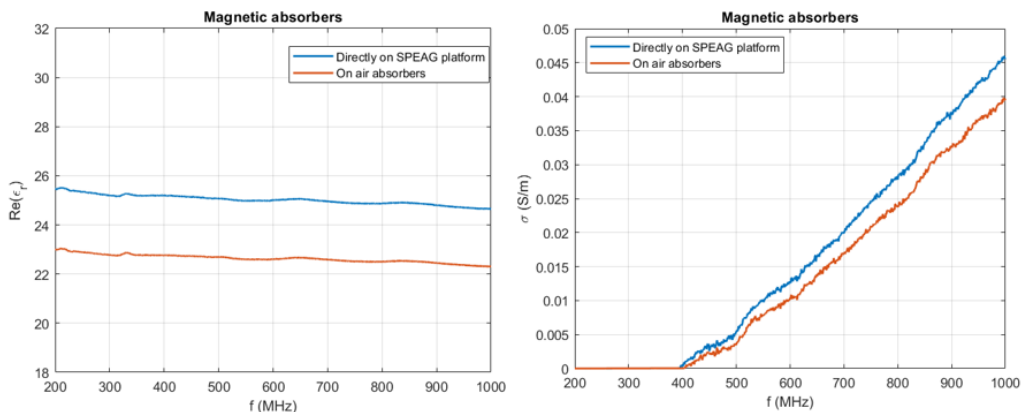


Figure 2.3: Magnetic absorbers characterization via probe. In blue, measurements are performed by directly placing the magnetic absorber layer on the SPEAG platform, while in red the magnetic absorber is placed on the foam absorber to increase the thickness of the layer tested.

Several configurations at the base of the model have been considered (as mentioned, one of the advantages of numerical simulations is the possibility of testing the same system under different conditions): the best focusing is achieved by placing at the base of the prototype only a muscle layer (simulating patient’s shoulders and with the same properties of agar-based mixture mimicking the neck muscle [33]), without any TBC or PEC condition. Then, the optimized phases resulting from this model have been provided as in-

put to a more realistic model of the experimental prototype which includes the Plexiglas base, a TBC, a PEC condition and foam absorbers (Figure 2.4); finally, the so obtained SAR and temperature maps are considered as a reference case to compare with experimental results.

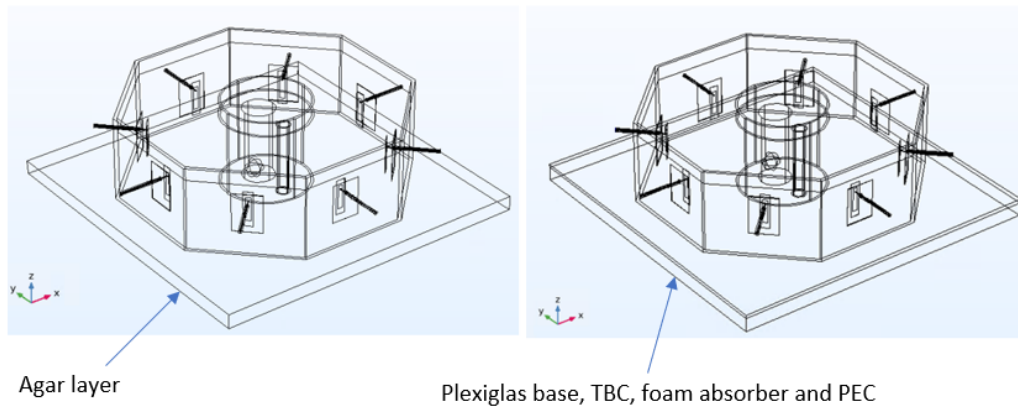


Figure 2.4: Agar layer at the base of neck prototype (left) and more “realistic” base (Plexiglas base, TBC, foam absorber and PEC) of the model (right).

Since the phased array is placed on  $xy$ -plane (parallel to the floor) at a certain height on the  $z$ -axis (perpendicular to the floor), controlling the focusing along the  $z$ -axis is not easy. However, it has been observed through simulations that the relative permeability value set in the TBC has a significant influence on  $z$ -axis focusing.

To mimic human neck tissue, agar-based mixture (polysaccharide extracted from red algae) is used: by adding the proper quantity of sugar, salt and agar powder to hot water [34] a gelatinous aggregate with dielectric characteristics close to those of human muscle was prepared.

In order to obtain more accurate numerical simulations, it is important to know the dielectric values of this agar-based compound with good precision, as well as to see how far these values deviate from those available in literature: differences between the dielectric parameters of the agar mixture (used as input values in the numerical models) and those taken from the literature could generate inaccuracies in the simulations (obtaining wrong phases, and, consequently, wrong temperature maps). Thus, an important part of the thesis is the evaluation of these parameters with a good precision (Section 4.4). For this reason, dielectric parameters of an agar compound sample have been evaluated at different depths (Figure 2.5) through a SPEAG probe [32] and given as input in COMSOL Multiphysics.

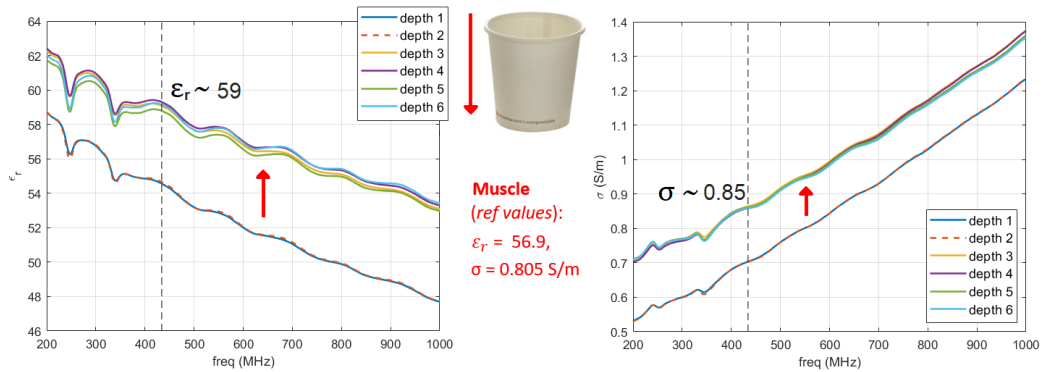
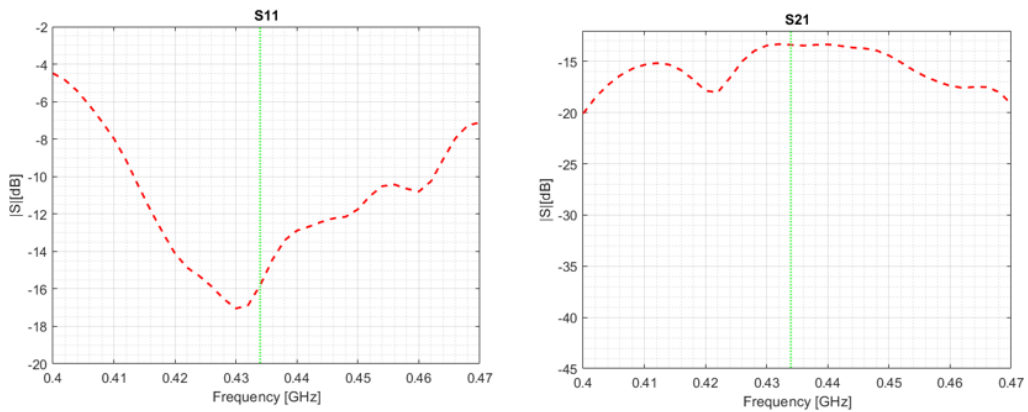


Figure 2.5: Dielectric characterization through a SPEAG probe.

The resulting values ( $\epsilon_r = 59$  and  $\sigma = 0.85$  S/m) are then set as input parameters in the numerical model.

## 2.3 S-parameters

Since S-parameters vary as a function of frequency, a study on their frequency dependence has been carried out in COMSOL Multiphysics: in particular, the study was conducted by supplying a unitary power to port 1 while keeping the other ports switched off (Figure 2.6).



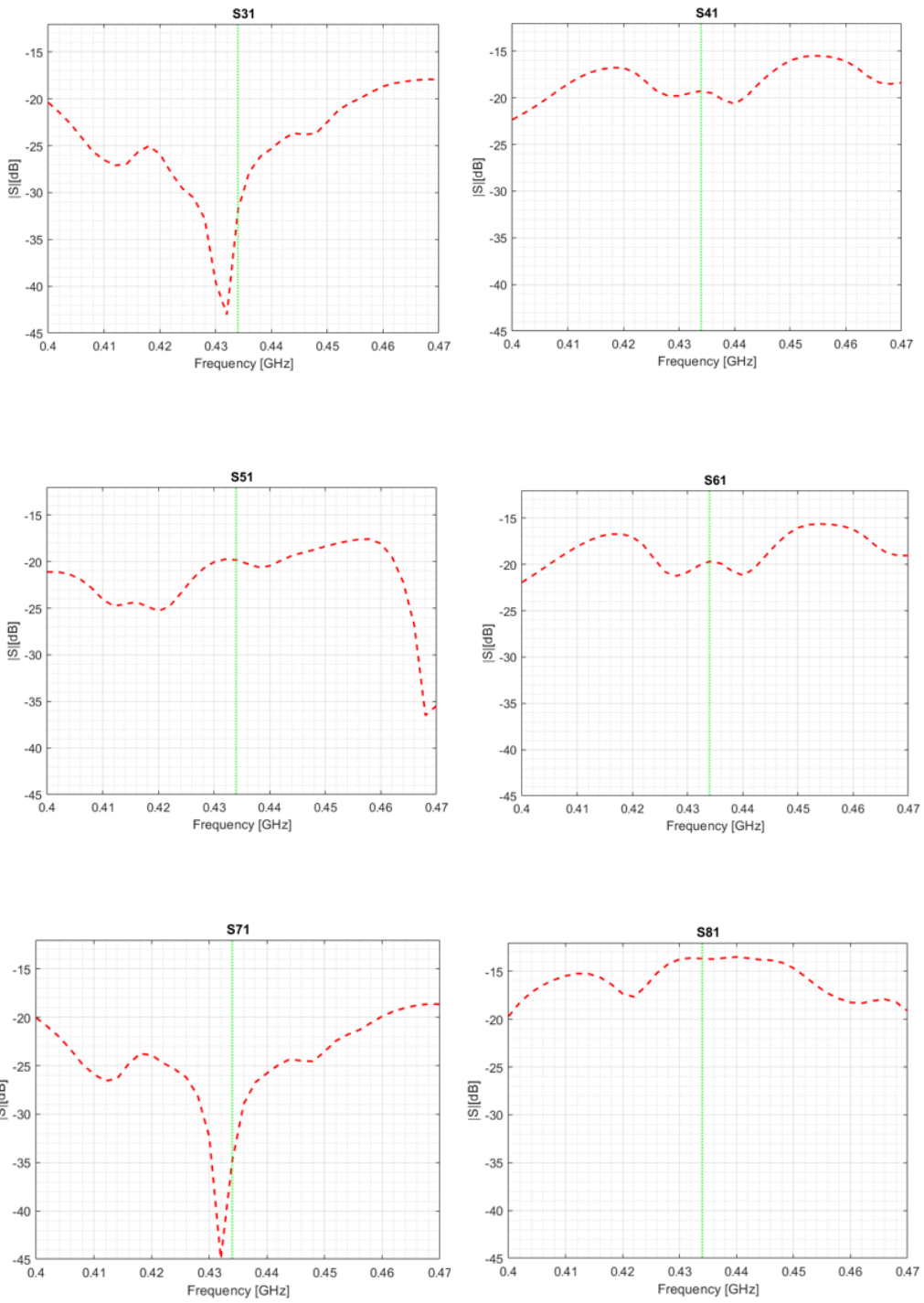


Figure 2.6: COMSOL analysis on S-parameters frequency dependence. A green dotted line marks the location of 434 MHz.

As can be seen from Figure 2.6, all transmission coefficients ( $S_{i1}$ , with  $i = 2, \dots, 8$ ) are smaller than -15 dB: converting this value to a linear scale, it means that about 15% of the power emitted by the antenna is reflected back, which we considered reasonable.

The reflection coefficient  $S_{11}$ , at the working frequency of 434 MHz (indicated by a green line) is also less than -15 dB (from the reflection coefficient curve it can be seen that the antenna has been optimized to work at a frequency of 434 MHz). Moreover, it should be noted that the antenna optimized with the simplified model (see Subsection 1.4.1) leads to good results also in the completed simulation model.

In Section 3.2, these COMSOL curves will be compared with those obtained experimentally.

## 2.4 SAR-based focusing

The optimization algorithm can be SAR-based [35] or temperature-based (T-based) [36], [17]: the T-based is the one that focuses directly on the quantity of interest (the temperature, T), but is more affected by the uncertainties on thermal characteristics of the tissues involved (especially perfusion) and requires more computation time than SAR-based optimization algorithms. Therefore, SAR-based has become widespread in clinical practice [15], and possible shifts of maximum in temperature maps due to thermal boundary conditions can be mitigated by add-on methods [17].

In particular, a SAR-based optimization exploits the fact that the total electric field generated by the array can be written as a linear superposition of the electric fields obtained for each antenna acting as standalone (i.e., when only one antenna is fed, while all the others are switched off):

$$\mathbf{E}_{tot} = \sum_{n=1}^{N_T} \tilde{v}_n \mathbf{e}_n, \quad (2.1)$$

where  $\mathbf{e}_n$  is the electric field generated by  $n$ -th antenna,  $\tilde{v}_n$  is the antenna feeding coefficients, and  $N_T$  is the number of antennas.

The SAR-based optimization (the one used in this thesis) aims at finding the antenna feedings that maximize the SAR (which is a function of the total field and, therefore, of the feedings) in a target region by minimizing the hot-spot-to-target SAR quotient (HTQ), defined as:

$$\text{HTQ} = \frac{\langle \text{SAR}_{V1} \rangle}{\langle \text{SAR}_{target} \rangle}, \quad (2.2)$$

where  $\langle \text{SAR}_{V_1} \rangle$  is the average SAR in the 1% of healthy volume  $V_1$  with the highest SAR, while  $\langle \text{SAR}_{target} \rangle$  is the average SAR evaluated in the target region (i.e., tumor location).

Using LiveLink™ for MATLAB®, a MATLAB code runs the COMSOL program, performs PSO optimization and returns in output the COMSOL program with the 8 optimized phases that minimize the HTQ. In particular, every time the algorithm is run:

1. each antenna is alternately switched on (with an unitary excitation of 1 V and phase  $0^\circ$ ) while all the others are switched off;
2. the electric field generated by the antenna turned on is calculated in both healthy and tumor regions;
3. the obtained fields are recombined with the respective feedings to define the objective function: through a linear combination of so calculated electric fields, an excitation-dependent function is derived;
4. the obtained function is what the algorithm minimizes.

The resulting optimized phases are given in input to the COMSOL program which returns the SAR and temperature maps in the optimum case.

Since having lower  $S_i^a$  active parameters (Subsection 1.4.2) means lower power reflected, another optimization algorithm which considers not only the focusing quality, but also the obtained active S-parameters has been implemented. In this case, the aim is to find the antenna phases that lead to a satisfactory temperature focusing on the target region, limiting the reflected power on each antenna. In particular, two different thresholds (-10 dB and -15 dB) on active S-parameters have been imposed: in this case the fitness function leads to a solution with high SAR in the tumor and a low SAR elsewhere, and, at the same time, keeps active S-parameters under the threshold. To do this, the fitness function (FF) considered has been defined as:

$$\text{FF} = \text{HTQ} + \sum_{n=1}^{N_T} f_n, \quad f_n = \begin{cases} 0 & \text{if } S_i^a \leq th_S \\ \frac{1}{N_T} & \text{if } S_i^a > th_S \end{cases}, \quad (2.3)$$

where  $N_T$  is the number of antennas,  $S_i^a$  is the active S-parameter of the  $i$ -th antenna, while  $th_S$  is a threshold (in dB) on the active S-parameters (-10 or -15 dB).

However, since the primary aim is to evaluate SAR focusing, the HTQ was also calculated and saved separately.

In this study, only the phase optimization is performed: the amplitude ( $v_n$ , with  $n=1,\dots,8$ ) is imposed to be the same for all the antennas ( $v_n = v_0 \forall n$ ), while the phases  $\varphi_n$  are optimized in their range from 0 to  $2\pi$ . So, antenna feedings ( $\tilde{v}_n$ ) can be written as:

$$\tilde{v}_n = v_n \exp(i\varphi_n) = v_0 \exp(i\varphi_n) . \quad (2.4)$$

The signal amplitude to give to each antenna ( $v_0$ ), is related to the total power supplied to the array ( $P_0$ ) by the relationship:

$$P_0 = \sum_{n=1}^{N_T} \frac{|\tilde{v}_n|^2}{2R_0} = \frac{v_0^2 N_T}{2R_0} \longrightarrow v_0 = \sqrt{\frac{2R_0 P_0}{N_T}} , \quad (2.5)$$

where  $R_0$  is the characteristic impedance equal to  $50 \Omega$  and  $N_T$  is the number of antennas ( $N_T = 8$ ).

The optimization of the phases is performed assuming  $P_0 = 1 \text{ W}$ ; once that the optimized phases are found, to increase the power (so, the generated temperature increase), it is sufficient to multiply the amplitude by  $\sqrt{P}$ , a dimensionless factor which indicates the total power given to the array (for example, in the studied case, a total power of  $40 \text{ W}$ ,  $5 \text{ W}$  for each antenna, is set, so the amplitude  $v_0$  is multiplied by  $\sqrt{40}$ ). A higher  $P$  implies a higher temperature in all the system as the dissipated power increases.

The optimization algorithm was tested by performing several simulations in COMSOL Multiphysics, obtained for different target positions.

This thesis presents also the experimental measurements (performed on an agar-based phantom mimicking the neck region) obtained using a set of feedings calculated on the basis of the simulation setup.

Results are then compared and analyzed in MATLAB (Subsection 4.2.1).

## 2.4.1 Particle Swarm Optimization

Particle Swarm Optimization (PSO) [37] is a global optimization algorithm inspired from the social behaviour of certain groups of animals such as birds or fishes in their quest for food. Two principles are at base of PSO: communication (so, the social component of the optimum research) and learning (the individual component).

As other Swarm Optimization algorithms, its main characteristics are: (1) the particles (i.e., candidate solutions) are based on simple formulas, (2) they cooperate indirectly and thus (3) are free to move in the solution space.

In particular, the parameters to set are:

- number of iterations: maximum number of iterations that the algorithm can perform (1000 as default in MATLAB);
- number of particles: how many particles will looking for the global optimum (100 in the considered case);
- the “inertia”, which tends to maintain the direction of the current  $i$ -th iteration;
- $c_1$ : the individual component (cognitive component), is the weight of the difference between the individual optimum found by  $n$ -th particle and its actual position;
- $c_2$ : the social component, weights the distance between the global optimum found by all particles up to that moment and the position of  $n$ -th particle.

# Chapter 3

## Experimental setup

The prototype, employed as realization of the numerical model, consists in a circular array of 8 patch antennas, whose dimensions has been optimized in CST (Subsection 1.4.1), organized around a Plexiglas cylinder mimicking the human neck structure. As shown in Figure 3.1, the aforementioned cylinder houses two cylindrical elements inside, which present different diameters and simulate trachea (hollow cylinder) and vertebral column (solid cylinder). Unlike the numerical model, in the experimental prototype no sphere was inserted to mimic the tumor: this study aims at focusing the temperature increase in a specific region of the phantom in which such a sphere would be inserted in a future project.

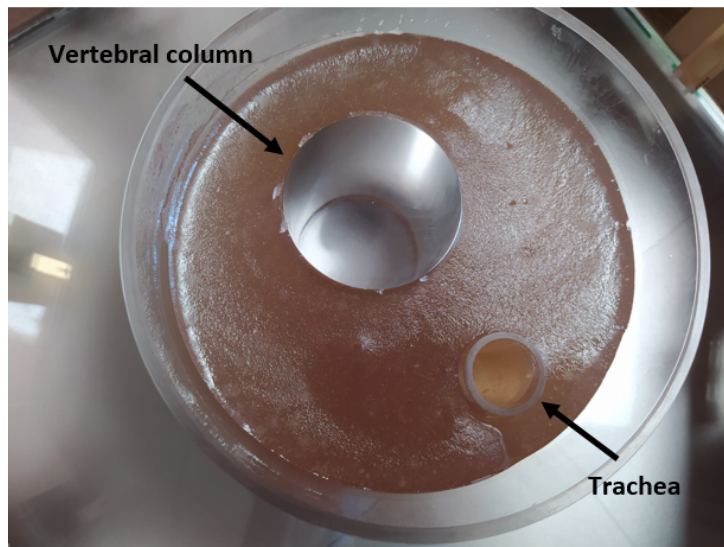


Figure 3.1: Cylinder prototype filled with agar-based mixture mimicking the human neck.

To simulate the waterbolus effect, the space around the cylinder mimicking the neck is filled with approximately 9 liters of demineralized water (Figure 3.2); this water also represents the real domain where the implemented antennas have been designed to operate (Subsection 1.4.1).

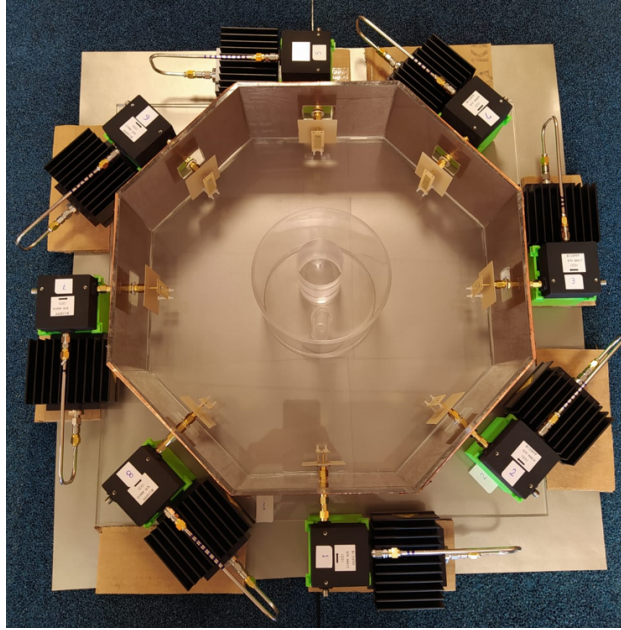


Figure 3.2: Circular phased-array (immersed in demineralized water) surrounding the neck prototype.

In the model definition, the following simplifying assumptions are considered:

- muscle tissue (mimicked by the agar) is homogeneous and isotropic;
- the effects of blood perfusion are neglected, they are not simulated;
- metabolic heat generation is neglected;
- the temperature of waterbolus is considered approximately constant.

Referring to the fourth point, a proper system has been implemented to keep the temperature of the water around the neck approximately constant:

(1) using a pump (flow rate 0.08 L/s) the water around the neck (in which the antennas are immersed) is aspirated, (2) then it passes through a 3-fan cooling system and finally, (3) the cooled water is put back inside the prototype (Figure 3.3).

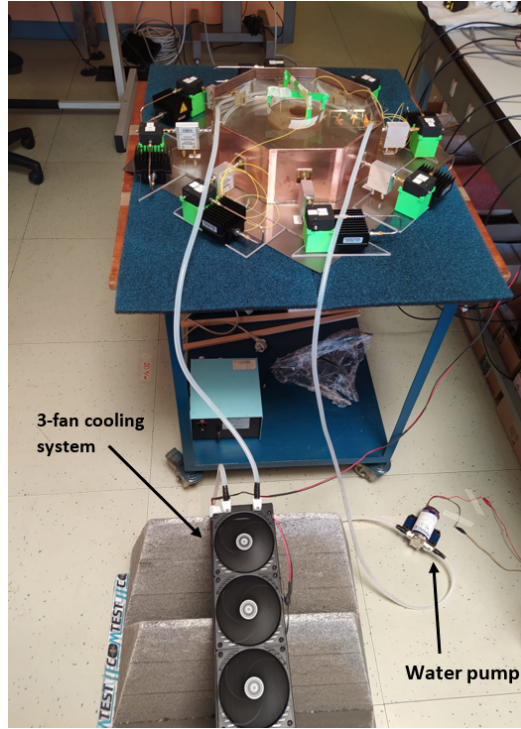


Figure 3.3: Complete experimental apparatus. In the foreground the 3-fan cooling system and the pump can be seen.

### 3.1 Electronic components

Each antenna of the circular phased-array surrounding the neck prototype is connected to a block composed by:

1. Phase Shifter (PS): provides, for each antenna, the proper offset<sup>1</sup> previously calculated with the optimization algorithm. In particular, these devices allow the introduction of a certain phase shift  $\phi$  by setting a proper voltage  $V_{ps}$ .
2. Variable Gain Amplifier (VGA): necessary to compensate losses (due to passive components) and gain fluctuations (due to active components). Because of the high sensitivity of VGA to the command voltage ( $V_a$ ), it is important to know the precise voltage given to each VGA.

---

<sup>1</sup>An important wave parameter, beside amplitude and frequency, is the phase. In general, phase has no meaning if referred to a single signal, but is observable when there are at least two signals at the same frequency. For example, in this thesis, 8 microwaves signals with the same amplitude and at the same frequency are shifted with respect to each other to obtain constructive interference in the target zone.

3. Power Amplifier (PA): amplifies with a high gain (approximately +40 dB) the signal delivered to each antenna.
4. Matched load ( $50 \Omega$ ): improves the matching to avoid that all the power goes back to the PA.

A signal generator provides the power to all the blocks, while a power splitter ideally divides this power among 8 output signals, one for each block.

Since each electronic component has its own uncertainties which must be analyzed for different functioning conditions, each channel (PS + VGA + PA) has been characterized by using a directional coupler and a power meter to measure the power on each channel while all antennas were functioning: in this way the actual amplitude given to each antenna is known (Figure 3.4). In particular:

- Directional coupler: couples a well-defined quantity of power to a port in one direction; in our case, it couples -20 dB of the input power to the power meter.
- Power meter (U2000 Series USB Average Power Sensors): connected to PC, and using the appropriate software (Keysight Benchvue software), it reads the power level. In particular, due to its limited maximum input power, only a part of the output power is measured (-20 dB, thanks to the directional coupler): therefore, the real output power will be equal to the measured power (in dB) + 20 dB.

Characterization of the block #n

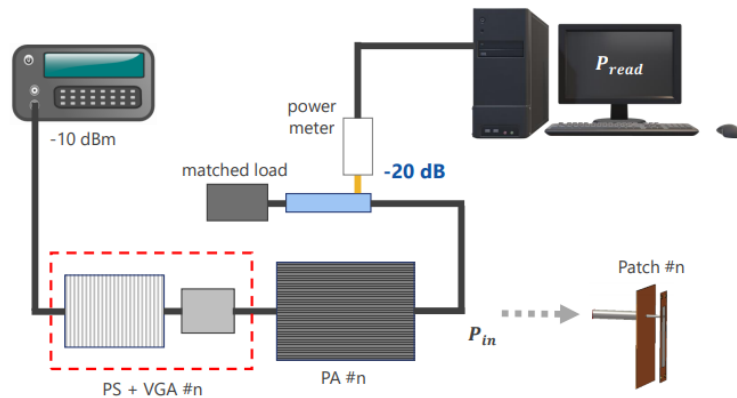


Figure 3.4: Scheme for power characterization of the  $n$ -th block.

Phase shifter and variable gain amplifier are both voltage controlled: by changing their voltages it is possible to vary the phase shift of the input signal and the channel's gain. In total, 16 voltages (two for each channel) are controlled through a DAC81416, i.e., a 16-channel digital-to-analog converter (DAC), and its respective support software DACx1416EVM Software.

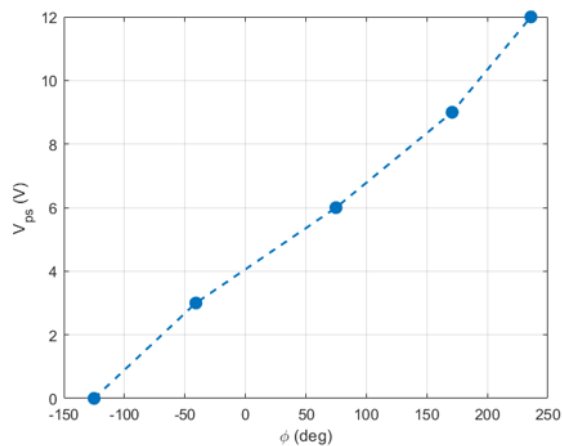
Once the proper phases have been obtained with PSO algorithm, it is necessary to determine the input control voltages of phase shifters ( $V_{ps}$ ) and variable gain amplifiers ( $V_a$ ). To this aim, a MATLAB interface that takes in input the required phases and provides in output the correct sequences of voltages  $V_{ps}$  and  $V_a$  has been developed (Figure 3.5).

Vps(V)	Vps(Hex)	Va(V)	Va(Hex)
7.514V	602D	1.32V	10E6
9.963V	7F88	1.268V	103A
0.6013V	0782	1.552V	13DC
1.295V	1095	1.288V	107C
11.25V	9004	1.358V	1163
7.599V	6144	1.302V	10AA
6.009V	4CEA	1.266V	1033
6.03V	4D30	1.503V	133D

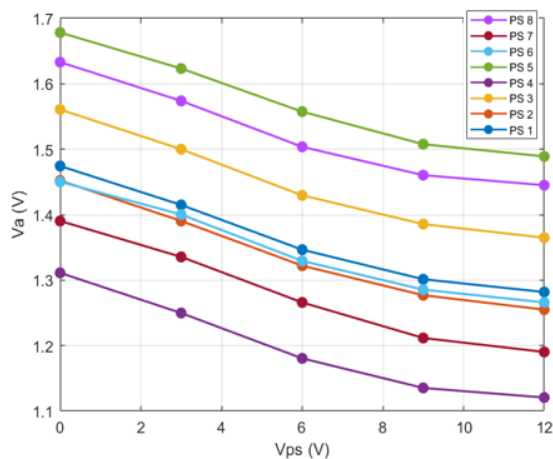
Figure 3.5: MATLAB application to obtain  $V_{ps}$  and  $V_a$ .

In particular, thanks to this MATLAB interface:

1. for each phase shifter, there is a specific experimental curve reporting phase shifters voltages ( $V_{ps}$ ) as a function of phase shift angles (Figure 3.6a);
2. for each phase shifter, once determined the control input voltage  $V_{ps}$ , another experimental curve, reporting the VGA command voltage ( $V_a$ ) as a function of  $V_{ps}$ , is considered (Figure 3.6b);
3. finally, the voltages values ( $V_a$  and  $V_{ps}$ ) determined in the previous steps are translated into the corresponding numerical values that identify that voltages on the DAC scale.



(a) Experimental curve  $\phi(V_{ps})$  for the  $n$ -th phase shifter.



(b) Experimental curves  $V_a(V_{ps})$  of all phase shifters.

Figure 3.6: Experimental curves to find the proper voltages  $V_a$  and  $V_{ps}$ .

Due to reflection problems of the power emitted from PA, a circulator (i.e., 3-ports non-reciprocal device) between the power amplifier and the antenna has been inserted: in this way, part of the reflected power from the antenna is transferred to the matched load of  $50 \Omega$  rather than to the power amplifier.

In particular, by putting the power meter in place of the matched load, it is possible to measure the reflected power from the antenna and so, by difference, knowing the actual power radiated from the antenna.

As all electronic components, also circulators have been characterized. In this case a Keysight's P937xA Series Vector Network Analyzer (VNA) was used: although the power meter allows to measure higher power<sup>2</sup>, it does not provide relative measures as VNA does (for example, the relationship between a given input and the corresponding output).

In particular, two different configurations have been tested (Figure 3.7): (a) port 1 and port 2 of the circulator connected to the VNA, and the “not measured” port (in this case, port 3) connected to a matched load; (b) port 1 and port 3 connected to the VNA, port 2 to the matched load. The configuration port 2 - port 3 is not tested as the circulator is always used with the input at port 1, so configurations (a) and (b) are sufficient to completely characterize the circulator.

An example of circulator characterization is reported in Figure 3.8.

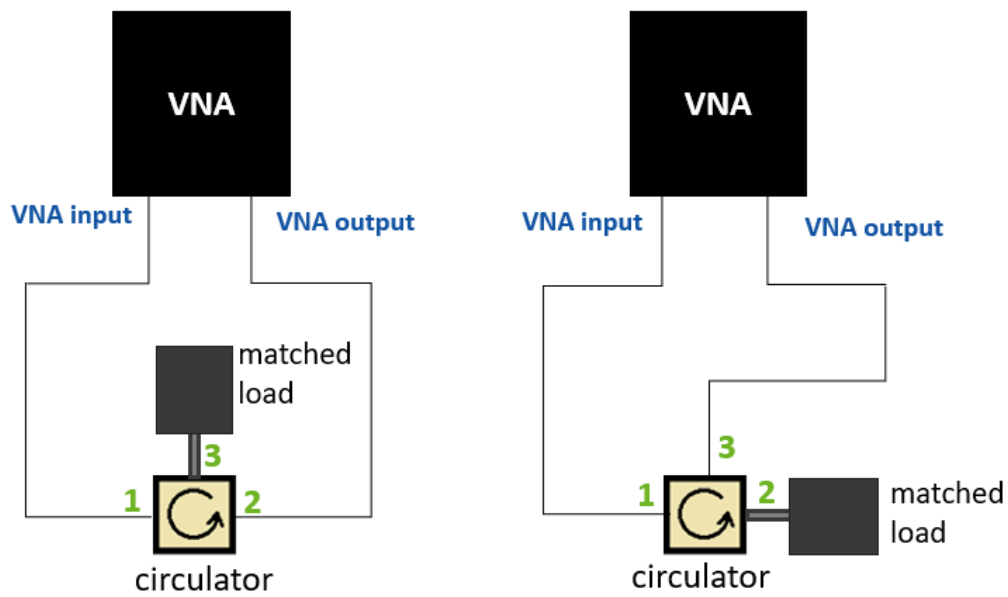


Figure 3.7: Scheme of the two configurations tested.

<sup>2</sup>The VNA can not measure high power, however, as circulators are linear devices (S-parameters do not depend on the power), their characterization can be done with lower power (few mW) than working power (few W).

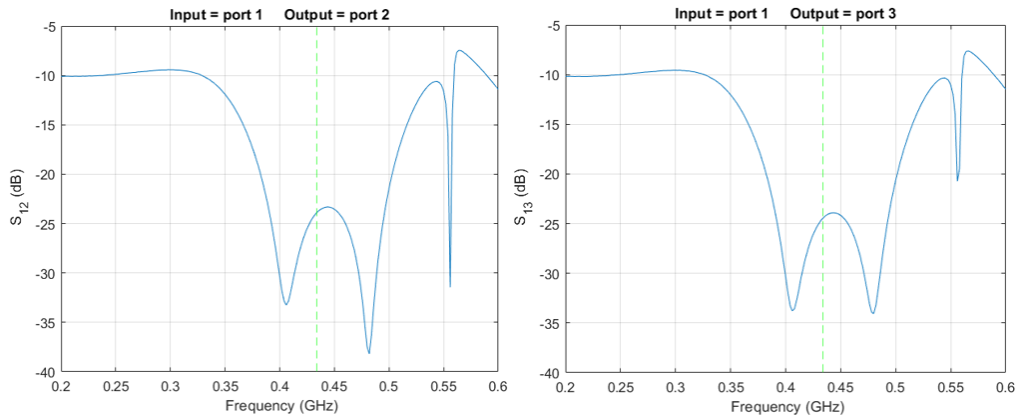
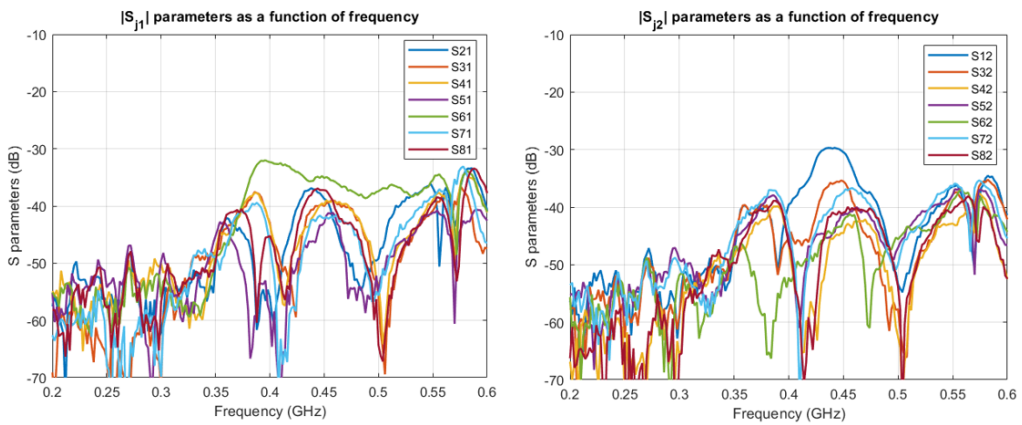


Figure 3.8: Example of circulator characterization. At 434 MHz the gain of the channel is less than -20 dB.

Two important points are: (1) the matched load seen by each power amplifier must be as constant as possible and (2) the cables must not affect too much the amount of power that is actually supplied to the antenna. For this reason, the transmission coefficients are evaluated: as can be seen from Figure 3.9 cables and all the electronic components before the antennas can be considered ideal from dissipation and losses point of view as their transmission coefficients are all smaller than -30 dB around 434 MHz.



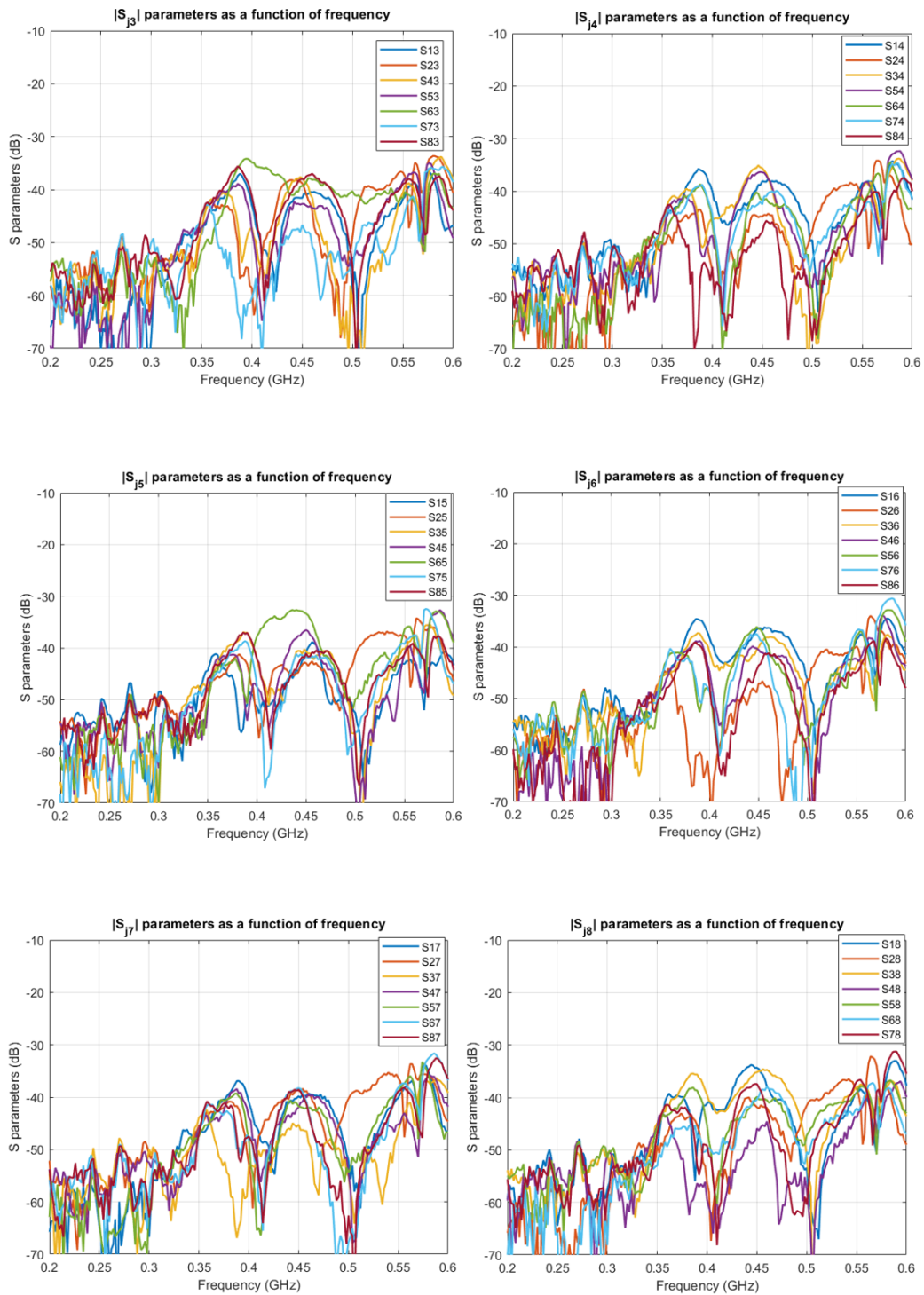
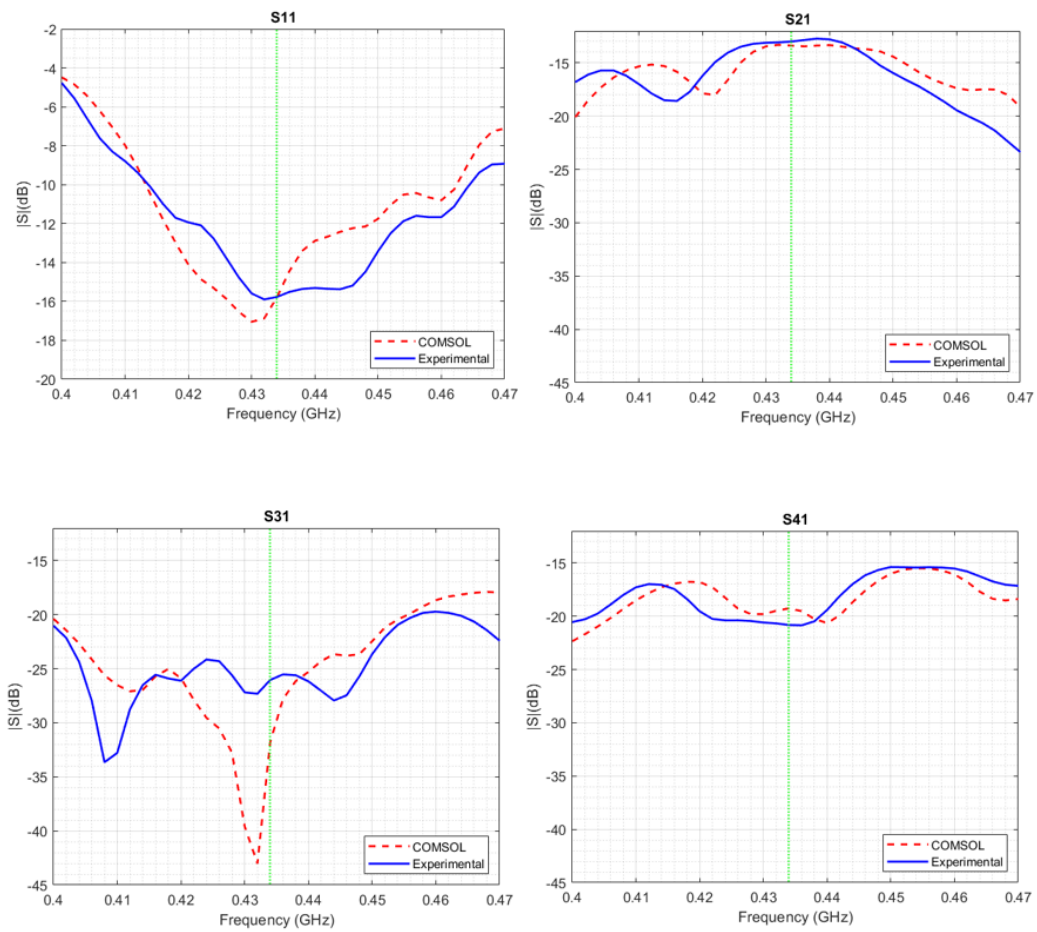


Figure 3.9: Transmission coefficients of each channel measured with the VNA in the presence of the circulators.

## 3.2 S-parameters characterization

In order to attest the validity of the COMSOL model, the frequency-dependent S-parameters obtained in COMSOL Multiphysics (Section 2.4) have been compared with those obtained experimentally (Figure 3.10).

In particular, experimental measurements are made with the VNA: antenna 1 is used as input (port 1), the remaining seven antennas as output (port 2), alternately. It is important to point out that the measurements used for this comparison have been carried out without circulators.



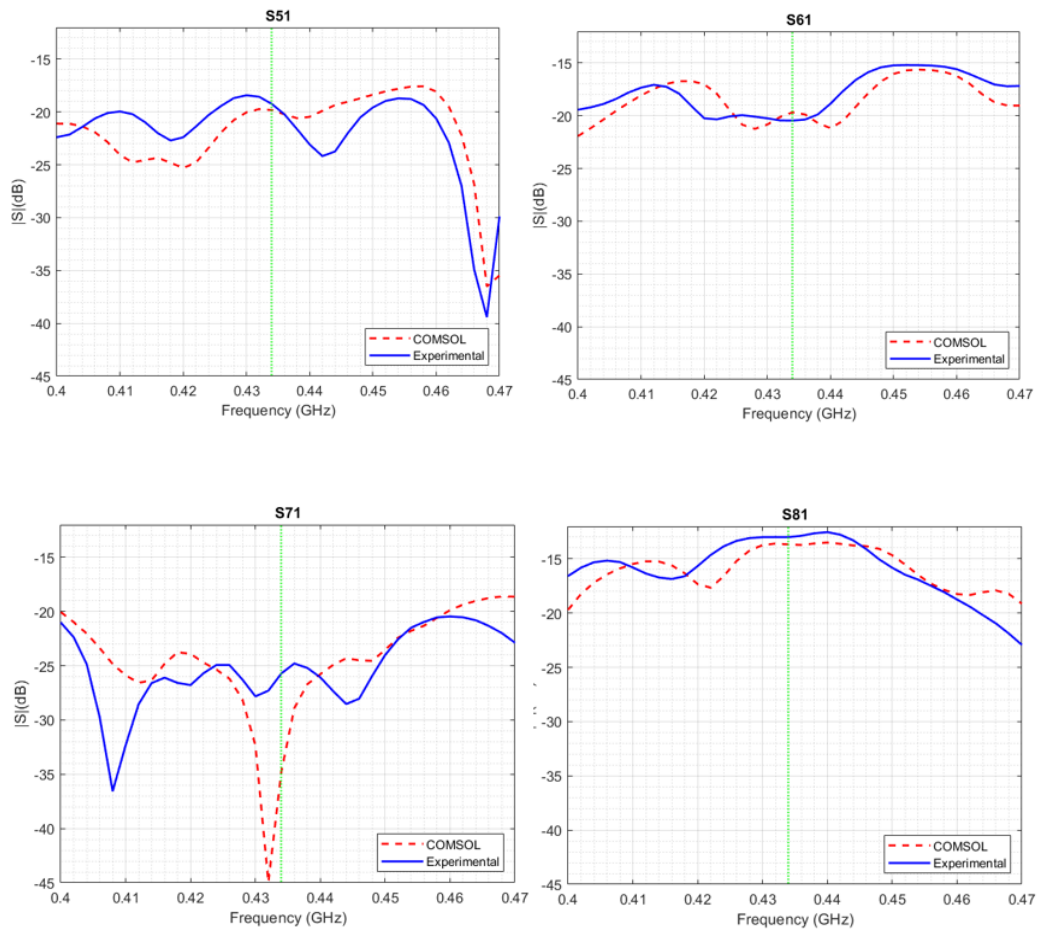


Figure 3.10: S parameters comparison: the dashed red line represents the parameters obtained in COMSOL Multiphysics, the solid blue line those measured experimentally. In particular, in this example, port 1 is fed, the others receive.

As can be seen from Figure 3.10, the curves in the two cases (simulation and experimental) are almost similar; in addition, lots of mismatch problems in the experimental (realistic) case are mitigated by circulators (whose purpose is to limit the non-ideal behaviour of the electronics components), leading to a better match between the simulation and experimental cases.

### 3.3 Radiofrequency electromagnetic field exposure guidelines

Since radiofrequency electromagnetic fields (EMFs) at high power levels can adversely affect human health, the International Commission on Non-Ionizing Radiation Protection (ICNIRP) published guidelines for human exposure to electromagnetic fields in the range from 100 kHz to 300 GHz [38].

The guidelines differentiate between occupationally-exposed individuals and general public: the former are defined as “*the adults who are exposed under controlled conditions associated with their occupational duties, trained to be aware of potential radiofrequency EMF risks and to employ appropriate harm-mitigation measures [...]*”; the latter is defined as “*individuals of all ages and of differing health statuses, which includes more vulnerable groups or individuals, and who may have no knowledge of or control over their exposure to EMF*” [38]. So, more stringent restrictions are applied for the general public, as they would not be trained to mitigate harm and not be aware about it.

Radiofrequency EMF levels corresponding to adverse health effects are defined as “basic restrictions”: reference levels have more conservative values than basic restrictions from which they derive.

In our case, we have considered the reference levels for occupationally-exposed individuals; in Italy, for this class, directive 2013/35/EU is applied through D.Lgs 159/2016. In particular, since the working frequency during the experiments was 434 MHz, frequency range from 400 MHz to 2000 MHz has been considered; in this range, the formula to find the reference value for the incident electric field (rms) is:

$$E_{lim} = 3 \times 10^{-3} f^{1/2} , \quad (3.1)$$

where  $f$  is the frequency expressed in Hertz.

Applying the expression (3.1) with  $f = 434 \times 10^6$  Hz we obtain a reference value equal to  $E_{lim} = 62.5$  V/m.

Prof. Aldo Canova (DENERG) kindly carried out the measurements using a proper probe (Figure 3.11): the electric field detected nearby the system around the antenna array fed with power  $P = 5$  W ranges from 15 V/m to 50 V/m.



Figure 3.11: Probe for electric field measure.

The measured electric field values has been written on the floor of the laboratory as a safety precaution: as can be seen in Figure 3.12, a rectangular region (in which the prototype is placed) has been delimited, and, although the calculated values are in compliance with directive 2013/35/EU, nobody was close to the system during its functioning.

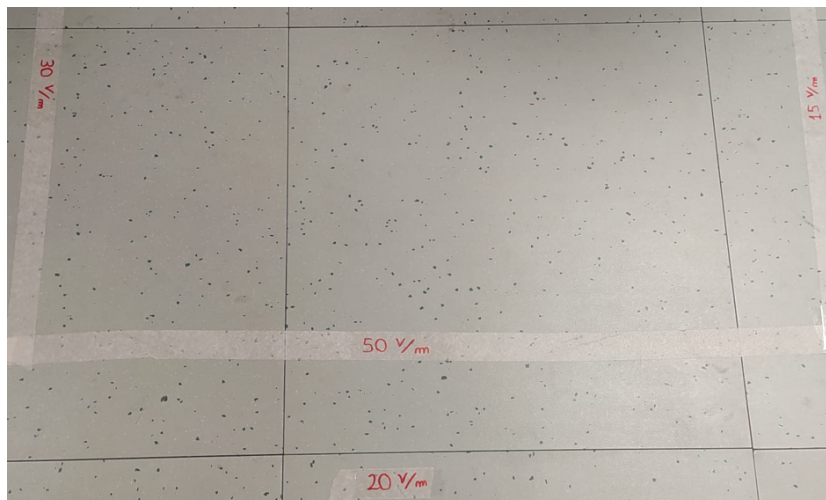


Figure 3.12: Electric field values written on the floor of the laboratory.

### 3.4 Temperature measurement setup

Temperature control during the treatment is fundamental for two reasons: on one hand, the clinical outcome of the hyperthermia treatment is strictly related to the thermal dose administered, so it is important that target temperature (tumor region) is neither too low (under 40 °C, the therapy has no effect) neither too high (over 46 °C, there is a risk of thermal ablation); on the other hand, the monitoring of the temperature in surrounding healthy tissues is important to avoid hotspots formation. For these reasons, a temperature control on the prototype has been performed by means of fiber-optic sensors and a thermal camera.

Currently, to monitor the internal temperature during the treatment, one of the most common methods is the use of fiber-optic sensors inserted into interstitial catheters (invasive method for the patient).

The only way to do non-invasive thermometry (NIT) is with functional magnetic resonance imaging (fMRI) [39], but the use of this technique in hyperthermia treatments is still in its infancy, given the cost and the need for an MRI machine: thermometry via fMRI requires the therapy to take place inside an MRI equipment, which would imply costs preventing widespread use in the clinic.

The simulation aspect (to simulate the geometry, the conditions as detailed as possible and see what happens) is also very important, but it is predictive, not the real situation to be measured. At the same time, in general, taking measurements on the real system always perturbs the system itself.

In the specific case, everything that has a conductor alters the electric field, so direct evaluation of the SAR is more sophisticated (a possible solution, for example, is the optical conversion, i.e., seeing the effect of a certain field on the optics). The other way of assessing SAR is often by direct thermal measurement (which, in the considered case, is also the result of most interest). However, even for measuring temperature there are some problems: thermocouples, for example, are made of conductive wires, so they alter and are altered by the electric field; therefore fiber-optic sensors and infrared cameras are used, although the latter have the limit of only seeing the external surface and not inside the object.

### 3.4.1 Fiber Bragg Gratings

A real-time system to monitor temperature distribution during the treatment is important to evaluate the correct focusing and to compare experimental temperature data with the simulated data.

In this thesis, two fiber-optic temperature sensors are used in two different positions: one along the position in which the tumor is located, the other in the mirrored position with respect to the neck axis ( $yz$ -plane) (Figure 3.13). In particular, two types of fibers have been used: a fiber inserted inside a glass capillary (greater stability, but risk of breakage during insertion of the fiber into the capillary) and a “bare” fiber (better sensitivity, but less stability). The setup of the fiber optics and their interrogator was carried out by Prof. Alberto Vallan, Prof. Guido Perrone and research fellow Aurora Bellone, who also helped us in the extrapolation and processing of the acquired data.

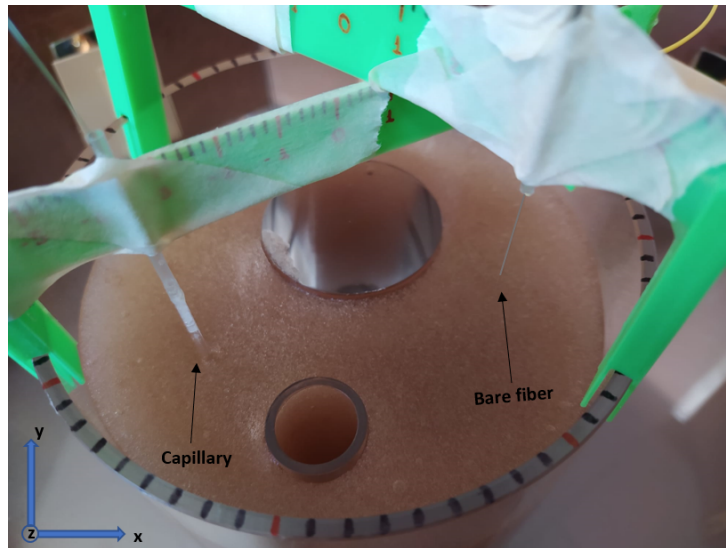


Figure 3.13: Fiber-optics inserted in agar mixture.

In this project, a Fiber Bragg Gratings (FBGs) sensor made by local modulation of the refraction index in the core of the fiber ( $n_{core}$ ) has been used (Figure 3.14). The light is reflected back near these local changes of  $n_{core}$  and, in particular, the reflection is maximum for a specific wavelength called Bragg wavelength  $\lambda_B$ , which can be evaluated as [40, 41]:

$$\lambda_B = 2n_{eff}\Lambda , \quad (3.2)$$

where  $\Lambda$  is the grating pitch (i.e., the distance between two neighbouring notches) and  $n_{eff}$  is the effective refraction index, which is equal to  $n_{eff} = n_{core}\sin\theta$  (being  $\theta$  the incident angle).

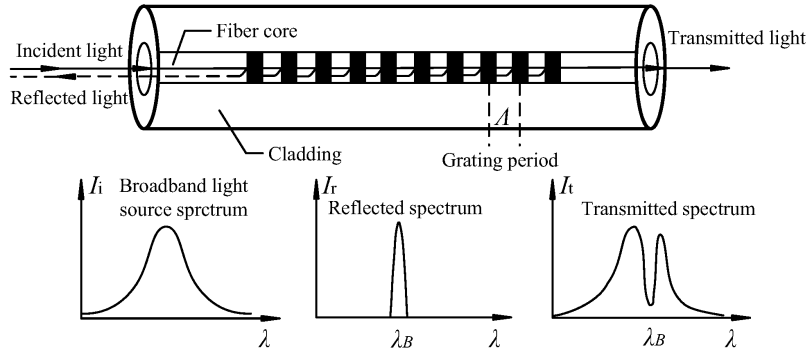


Figure 3.14: Fiber Bragg Gratings functioning principle [42].

The equation (3.2) implies that Bragg wavelength changes if refractive index or grating pitch (or both) changes. For example, if a mechanical stretch occurs,  $\Lambda$  changes, so  $\lambda_B$  will be different. Similarly, a temperature variation will affect both the pitch (thermal expansion) and the refractive index (thermo-optic effect), and so the value of Bragg wavelength.

By measuring the shift of  $\lambda_B$  ( $\Delta\lambda_B$ ), and knowing the coefficient of thermal expansion ( $\alpha$ ) and thermo-optic coefficient ( $\zeta$ ), the temperature variation can be obtained by applying the following relation:

$$\Delta\lambda_B = \lambda_B(\alpha + \zeta)\Delta T, \quad (3.3)$$

in which  $\alpha$  and  $\zeta$  are measured in  $^{\circ}\text{C}^{-1}$ .

So, by acquiring (in the specific case, with a sample frequency of 10 Hz) Bragg wavelength through an optical interrogator, the temperature variation can be measured.

Fiber Bragg Gratings sensors present lots of important advantages compared to other electrical sensors [43, 44]: they are corrosion resistant, transmit the signal for long distances without distortions, and, very important for our aim, FBGs are immune to electromagnetic interference.

In particular, some specifications of the optical fiber used for the thesis are:

- Array of 20 FBGs.
- Distance between adjacent FBGs: 2 mm.
- Array length: 4 cm.
- Wavelength of incident light  $\lambda = 1505$  nm.

To obtain the slope and the intercept of the calibration curve, the system was calibrated connecting the optic-fibers to the interrogator (Micron Optics HYPERION si155) and measuring the cooling phase of an aluminium block from about 70-75 °C down to 40 °C.

### 3.4.2 Thermal imaging camera

The thermal imaging camera is an instrument that measures the infrared (IR) radiation emitted by atoms and molecules in their thermal agitation: the emitted IR radiation is collected by an array of infrared detector elements which generate the thermogram (i.e., a false-color image of the framed object).

Starting from its emission spectrum, the temperature of the framed body can be obtained applying Planck's law and Wien's displacement law: the former describes the power per unit area (radiance) emitted by a black body at a certain temperature for different wavelengths, the latter establishes a relationship between the position of the emission peak and the temperature. In particular, the Planck's law is [45]:

$$W_\lambda = \frac{c_1}{\lambda^5 \cdot [e^{\frac{c_2}{\lambda \cdot T}} - 1]}, \quad (3.4)$$

where  $W_\lambda$  is the spectral radiant emittance ( $\text{W}/(\text{m}^3 \cdot \text{sr})$ ),  $\lambda$  is the wavelength (m),  $T$  is the temperature of the black body (K), while  $c_1$  ( $\text{J}/\text{s}$ ) and  $c_2$  ( $\text{m} \cdot \text{K}$ ) are two constants. The resulting curves are reported in Figure 3.15.

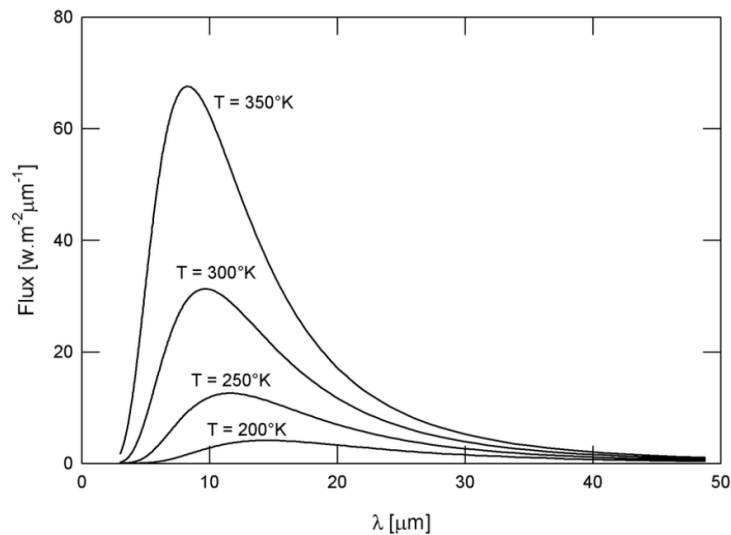


Figure 3.15: Curves obtained applying Planck's law [46].

According to Wien's law [47], the peak position ( $\lambda_P$ ) depends on temperature:

$$\lambda_P \cdot T = 2898 \mu m \cdot K , \quad (3.5)$$

thus, by measuring the wavelength of the peak radiance, it is possible to determine the temperature of the examined object. The information acquired and processed by the camera are then represented on the display with different colours according to the intensity of infrared emissions and, consequently, temperature.

For example, Figure 3.16 shows the action of the pump (water recirculation and cooling) observed using the thermal camera: as can be seen, the warmer water is replaced by cooler one (darker in the Figure).

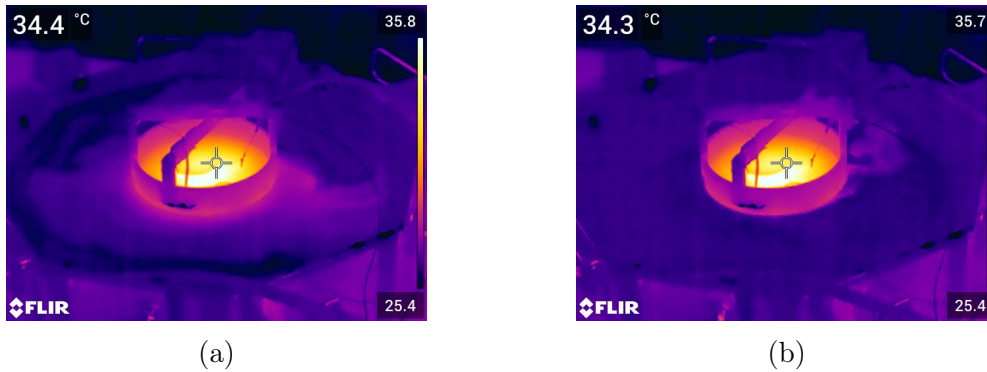


Figure 3.16: Pump effect seen through thermal camera.

Some of the main specifications of a thermal camera are: (1) the object temperature range, (2) the sensitivity, (3) the accuracy and (4) the image frequency.

In particular, the thermal camera used (FLIR<sup>®</sup> E54) presents the following specifications:

- Object temperature range: -20 to 120 °C; 0 to 650 °C.
- Thermal sensitivity: < 40 mK at 30 °C.
- Accuracy:  $\pm 2\%$  of the reading.
- Image frequency: 30 Hz.

# Chapter 4

## Heating session results

### 4.1 SAR focusing in COMSOL Multiphysics

Several situations with different parameters have been simulated in COMSOL Multiphysics: the situation leading to a better SAR focusing in the target region (i.e., a sphere with diameter  $d = 25$  mm centered in  $(x_t, y_t, z_t) = (-30, -15, -15)$  mm mimicking the tumor) is the one with just a 20 cm muscle layer at the base of the neck instead of the Plexiglas base and the absorbers (Figure 4.1).

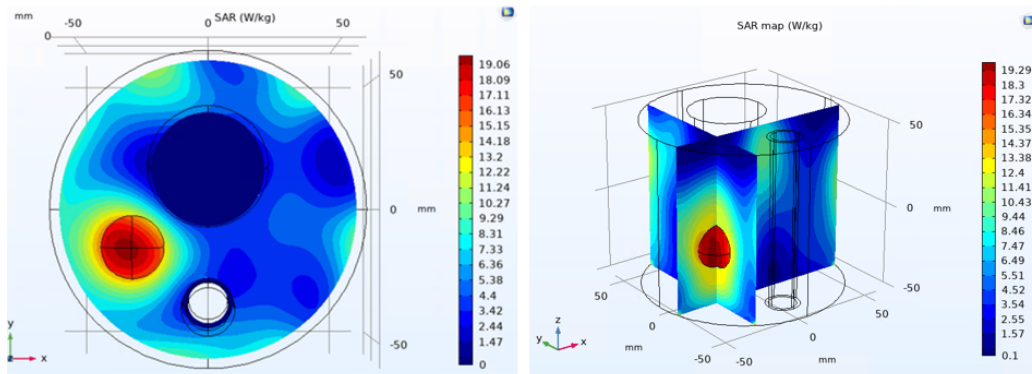


Figure 4.1: SAR maps on  $xy$ -plane (left) located at  $z = z_t$  (where  $z_t$  is the  $z$ -coordinate of the tumor center), and  $xz$ -  $yz$ -planes (right) obtained with a 20 cm muscle layer at the base of the neck prototype.

Starting from this ideal situation and imposing a threshold  $S_{th} = -10$  dB on the resulting active S-parameters, the optimized phases, shown in Table 4.1, have been obtained.

ant1	ant2	ant3	ant4	ant5	ant6	ant7	ant8
325.25°	60.24°	121.29°	141.45°	90.15°	360.18°	299.36°	297.73°

Table 4.1: Optimized phases obtained with 20 cm muscle layer at the base of the neck prototype.

These phases are then given in input to a COMSOL program simulating a more realistic situation, which presents at the base of the neck prototype: (1) a Plexiglas base, (2) a Transition Boundary Condition (TBC) simulating magnetic absorbers, (3) microwaves absorbing foam and finally, (4) PEC condition simulating the metallic table on which the entire prototype is placed. The so obtained SAR distributions are well-focused on the target region both on  $xy$ -plane (Figure 4.2, left) and  $yz$ -plane (Figure 4.2, right).

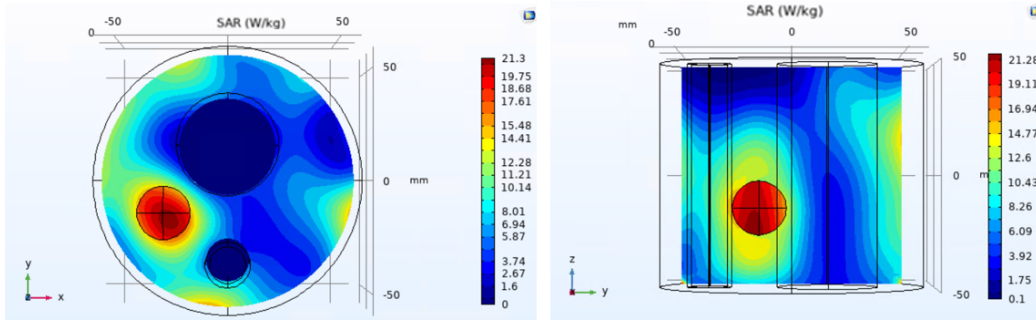


Figure 4.2: SAR distribution on  $xy$ -plane (left) and  $yz$ -plane (right) obtained with the “realistic” numerical model.

## 4.2 Temperature maps

Starting from the obtained SAR maps and solving the bioheat equation (1.8), the corresponding temperature maps have been computed: considering the “ideal” case (muscle layer at the base of the prototype), a good temperature focusing on the target region has been reached (Figure 4.3); nevertheless the temperature increase tends to overflow upwards and downwards (around the region of interest) along the vertical direction.

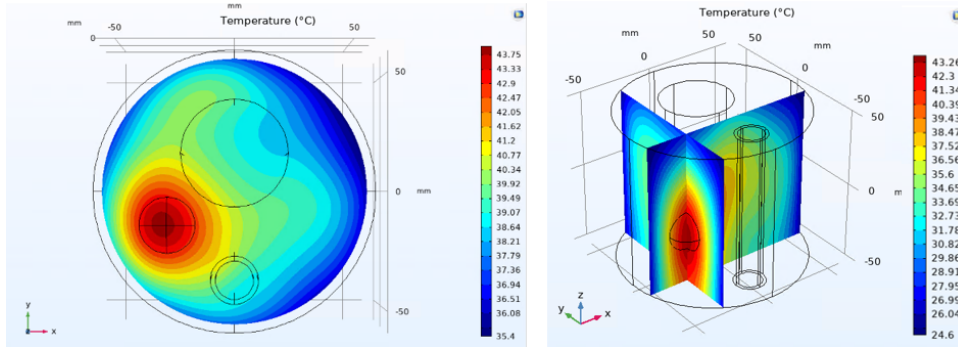


Figure 4.3: Temperature distribution on  $xy$ -plane (left) and on the  $xz$ -  $yz$ -planes (right) obtained with the “ideal” numerical model (muscle layer at the base of the prototype).

In the more realistic situation, a good focusing has been reached on the  $xy$ -plane (Figure 4.4, left) and  $xz$ -plane (Figure 4.4, right) despite a slight temperature increase around the target region.

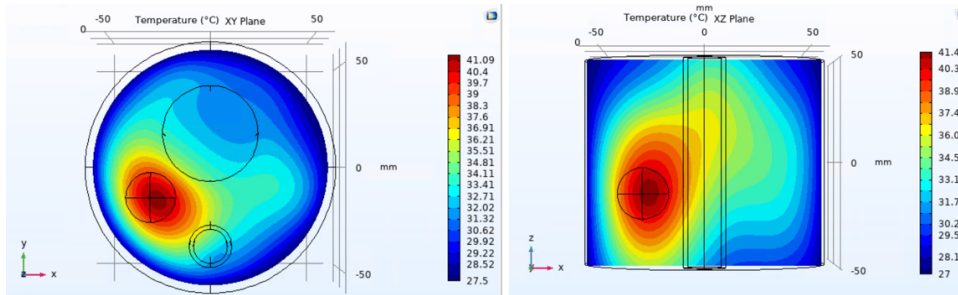


Figure 4.4: Temperature distribution on  $xy$ -plane (left) and on  $xz$ -plane (right) obtained with the “realistic” numerical model.

The reason of this shift could be related to the thermal boundary conditions: it was not possible to quantify precisely the heat exchange that the prototype and its elements (e.g., the cylinder mimicking the trachea or the upper agar surface) have with the external environment and how much this exchange affects the results.

In addition, since the phased array is designed to optimize on  $xy$ -plane, to manage the focusing along  $z$ -axis is more difficult.

To have a better temperature control along  $z$ -axis (neck axis), at least two circular arrays would be necessary: for example, the HYPERcollar [4] used for hyperthermia treatments in the neck region has two concentric circular arrays of 6 antennas (more complex system than the one considered in the thesis) which allow to better control the focusing also along the neck axis.

### 4.2.1 Temperature maps comparison

To make comparisons, once the temperature maps via numerical simulations have been obtained, the temperature distribution was evaluated experimentally through two fiber-optic sensors (Subsection 3.4.1).

A crucial part of the experimental temperature measurement was the insertion of the fibers in the agar mixture: since the gratings are sensible not only to the temperature, but also to the strain (Subsection 3.4.1), it is important to insert the fiber as straight as possible. To this aim, one fiber has been inserted in a glass capillary tube (Figure 4.5): in this way, its mechanical stability increases without decreasing its sensing capacity.



Figure 4.5: Fiber-optic sensor inserted in a capillary used to measure temperature.

The other “bare” fiber was too affected by strains, leading to unreliable temperature measurements: therefore, the only measurements that have been compared with the simulations were those acquired with the fiber inserted in the capillary along a line parallel to the  $z$ -axis and passing through the center of the tumor  $(x_t, y_t, z_t)$ .

In the considered experiment, since the agar-based mixture is prepared using high temperatures (up to 90 °C), it is important to let the system cool to obtain an almost uniform temperature distribution: for this reason, in general, the acquisitions were performed one or two days after the agar preparation.

Figure 4.6 shows an example of the acquired temperature for an entire warm-up session: to check that the curves are overlapped (i.e., the agar temperature is almost uniform in the whole neck structure and corresponds to the one measured by a thermocouple) 20 minutes of acquisitions with all the antennas turned off are performed (red bracket in Figure 4.6 indicates the final fraction of these 20 minutes).

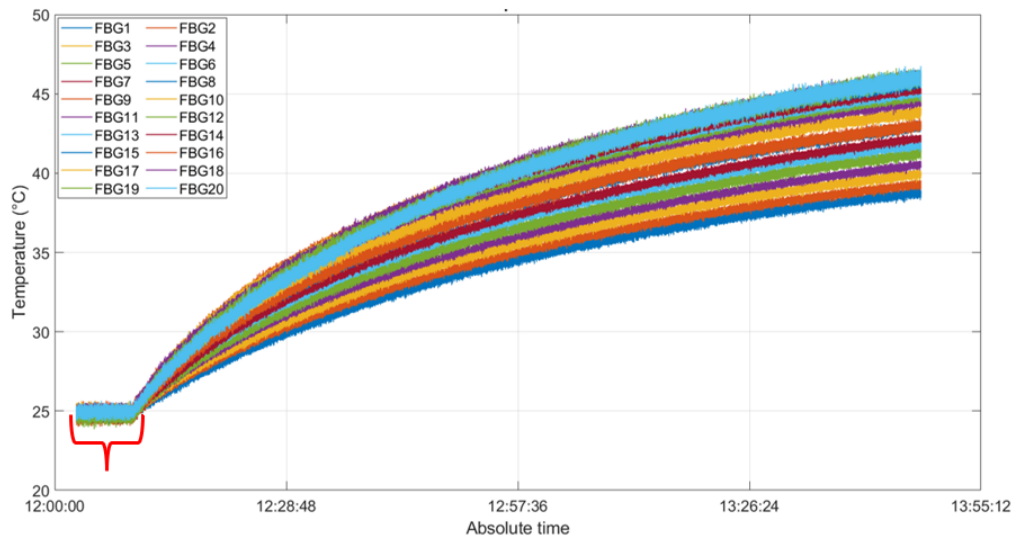


Figure 4.6: Curves of temperature variation in time obtained acquiring the Bragg wavelength through an interrogator. Red bracket indicates the final fraction of 20 minutes of acquisitions with all the antennas turned off.

Comparison between the experimental results (obtained using the fiber in the capillary) with the ones obtained in COMSOL Multiphysics (Figure 4.7) shows a difference of up to 2 °C in the temperature reached. This mismatch could be due to five potential sources of error: (1) temperature sensor’s uncertainties (approximately  $\pm 1$  °C); (2) malfunctions in the electronic setup; (3) uncertainties on the actual magnetic and dielectric parameters of the absorbers at the base of the prototype; (4) knowing with low precision the position of the fiber sensing zone; (5) wrong thermal parameters of the agar-based compound used in the model.

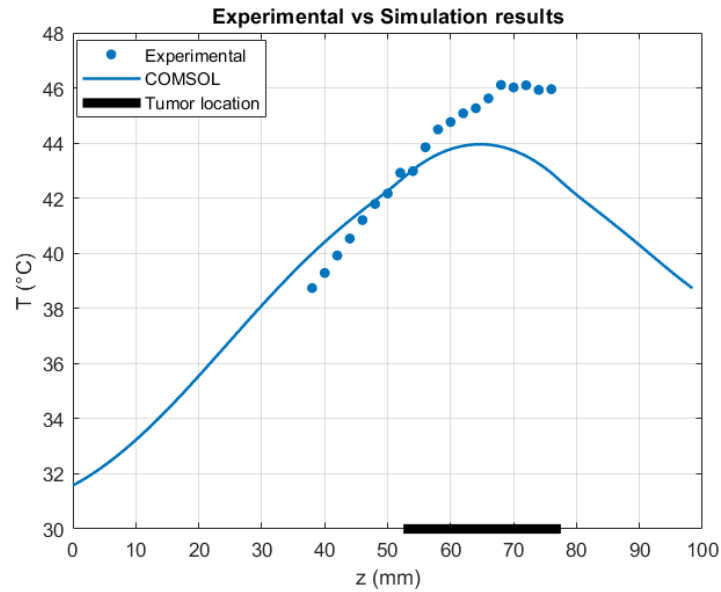


Figure 4.7: Comparison between experimental and COMSOL data.

The effect of the water around the neck allows the system to converge more quickly to a stationary state. The time-dependent temperature profile along a line parallel to the  $z$ -axis passing through the tumor center has been computed in COMSOL Multiphysics (Figure 4.8): the distance between two consecutive curves decreases in time as the temperature converges.

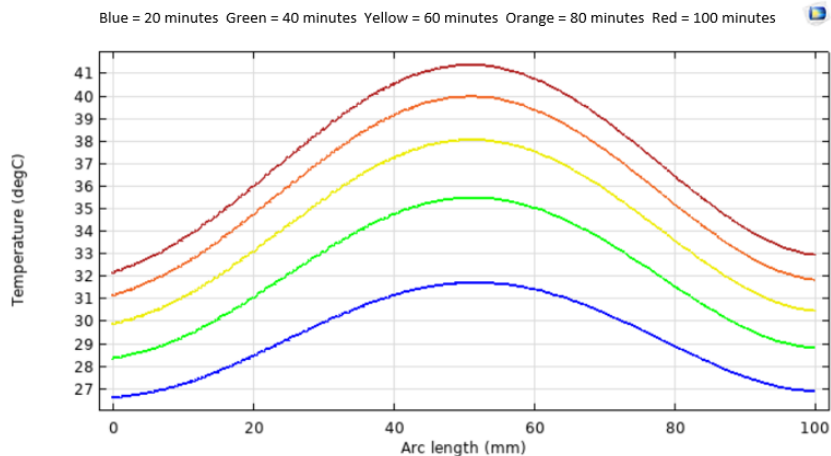


Figure 4.8: Time-dependent temperature along the  $z$ -axis (steps of 20 minutes) obtained in COMSOL Multiphysics.

### 4.3 Thermal characterization

Due to the observed difference between experimental and simulation case and due to the high variability and the high number of parameters that influence the final results, a thermal characterization on square agar samples (Figure 4.9) has been performed.



Figure 4.9: Agar samples for thermal characterization.

The measurements have been carried out by Prof. Alberto Fina and Dr. Daniele Battagazzore, at DISAT (Department of Applied Science and Technology) in Alessandria.

In particular, a coil placed in contact with the sample to be characterized between well-known temperature sources has been used. Then, the resistance  $R$  of the coil which is a function of the temperature  $R(T)$  is measured, thus obtaining information on the dissipated heat in the sample.

The measured thermal conductivity is  $0.60 \pm 0.03 \text{ W}/(\text{m} \cdot ^\circ\text{C})$  at  $23 \text{ }^\circ\text{C}$  and almost the same at  $37 \text{ }^\circ\text{C}$  ( $0.59 \pm 0.03 \text{ W}/(\text{m} \cdot ^\circ\text{C})$ ). The error band indicated results from repeated measurements on the same sample: in reality, the real error on the measurements may be a little higher due to the presence of some bubbles in the sample (even if they were small and uniformly distributed); the value may also change slightly depending on the measurement conditions.

To measure heat capacity, the classical method via DSC (ASTM E1269)<sup>1</sup> [48]

---

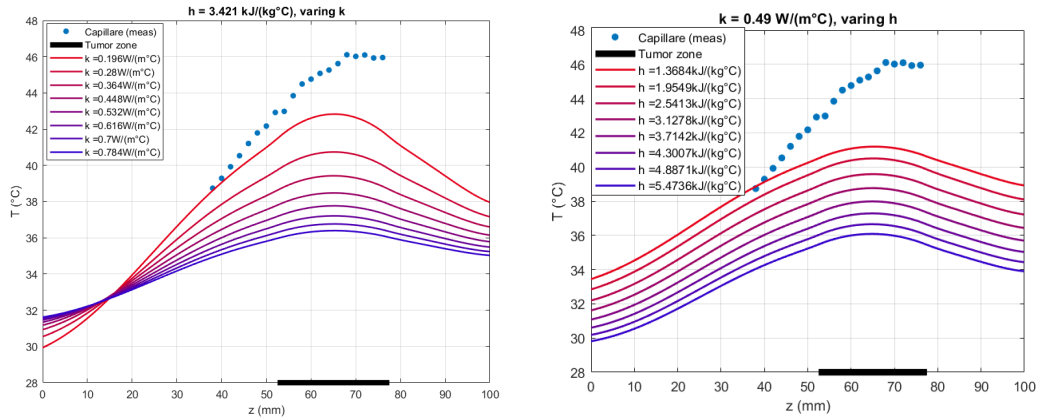
<sup>1</sup>This test method is under the jurisdiction of ASTM Committee E37 on Thermal Measurement and is the direct responsibility of Subcommittee E37.01 on Test Methods and Recommended Practices. Current edition approved Feb. 10, 2001. Published April 2001. Originally published as E 1269–90. Last previous edition E 1269–99.

has been applied on the two agar samples of approximately square shape and 4 cm thickness prepared according to the same proportions used for the prototype. Several tests were carried out: the obtained values were repeatable and in the range of  $3.1 \pm 0.1 \text{ J}/(\text{g} \cdot \text{K})$  at room temperature. The measurement was not carried out also at  $37 \text{ }^\circ\text{C}$  because there could be a loss of water from the agar mixture; however, since the obtained curve was nearly flat, the result should be almost the same.

Moreover, a simulation analysis about the influence of agar thermal conductivity  $k$  and heat capacity  $h$  on the results was performed. The nominal values of the heat capacity  $h_{nom}$  and the thermal conductivity  $k_{nom}$  for the muscle tissues were considered (from the IT'IS database,  $h_{nom} = 3.421 \text{ kJ}/(\text{kg} \cdot \text{ }^\circ\text{C})$  and  $k_{nom} = 0.490 \text{ W}/(\text{m} \cdot \text{ }^\circ\text{C})$ , respectively).

In particular, 8 COMSOL simulations were run only varying their values of predefined quantities:

- Heat capacity was varied from  $h_{min} = h_{nom} - (0.6 * h_{nom}) = 1.368 \text{ kJ}/(\text{kg} \cdot \text{ }^\circ\text{C})$  to  $h_{max} = h_{nom} + (0.6 * h_{nom}) = 5.474 \text{ kJ}/(\text{kg} \cdot \text{ }^\circ\text{C})$ .
- Applying the same criteria, the thermal conductivity was varied from  $k_{min} = k_{nom} - (0.6 * k_{nom}) = 0.196 \text{ W}/(\text{m} \cdot \text{ }^\circ\text{C})$  to  $k_{max} = k_{nom} + (0.6 * k_{nom}) = 0.784 \text{ W}/(\text{m} \cdot \text{ }^\circ\text{C})$ .



(a) Thermal conductivity variation.

(b) Heat capacity variation.

Figure 4.10: Temperature distribution along  $z$ -axis in tumor location by varying the thermal conductivity  $k$  and the heat capacity  $h$ .

As can be seen in Figure 4.10, heat capacity variation implies just a translation (the curve trend does not change), while the variation of the

thermal conductivity leads to a different slope of the curves. In particular, the lower is  $k$ , the higher is the slope: the reason is that in Pennes equation (1.8) there is the the product between the thermal conductivity  $k$  and the temperature gradient.

In conclusion, the higher is the thermal conductivity, the faster the heat distributes in the agar, leading to a flatter curve (so, more uniform) of the temperature distribution along the  $z$ -axis.

#### 4.4 Dielectric characterization: error analysis

The measurement of dielectric properties is a fundamental step to obtain more realistic models and predictions: as well as knowing the dielectric parameters of the muscle is important for a good treatment [49, 50], it is also important to obtain precise simulations.

The dielectric characterization (i.e., the evaluation of complex permittivity, which includes both relative permittivity and electrical conductivity) is carried out through a coaxial probe (Figure 4.11): by measuring the reflection coefficient ( $S_{11}$ ) with the VNA at the working frequency of 434 MHz it was possible to obtain the complex permittivity of the agar  $\tilde{\epsilon}_a$ .



Figure 4.11: Agar characterization with a coaxial probe.

#### 4.4.1 Marsland and Evans method

In particular, to obtain the permittivity of the medium from  $S_{11}$ , Marsland and Evans [51] proposed the following equation:

$$\tilde{\epsilon}_a = -\frac{\Delta_{13}\Delta_{m2}}{\Delta_{32}\Delta_{m1}}\tilde{\epsilon}_3 - \frac{\Delta_{21}\Delta_{m3}}{\Delta_{32}\Delta_{m1}}\tilde{\epsilon}_2, \quad (4.1)$$

which is based on 3 calibrations: (1) short circuit, (2) open-ended and (3) distilled water. The terms  $\Delta_{ij} = S_{11,i} - S_{11,j}$  are the reflection coefficients measured during the calibrations ( $i = 1, 2, 3$ , with 1 = short circuit, 2 = open-ended, 3 = distilled water), while  $\Delta_{mi}$  is equal to  $S_{11,m} - S_{11,i}$ , where  $S_{11,m}$  is the reflection coefficient measured in the agar.

So, before obtaining the measurements, a calibration in fluids (air and distilled water) with well-characterized properties is necessary. In particular, the relative permittivity of the water has been considered equal to  $\epsilon'_{r,water} = Re(\tilde{\epsilon}_3) = 79.5$ , while the electrical conductivity  $\sigma_{water} = Im(\tilde{\epsilon}_3) = 0.047$  S/m.

Once evaluated the complex permittivity with expression (4.1), since it is defined as:

$$\tilde{\epsilon}_a = \epsilon_0 \left( \epsilon_r - i \frac{\sigma}{\omega \epsilon_0} \right), \quad (4.2)$$

the relative permittivity and the electrical conductivity can be obtained by considering the real and the imaginary part of  $\tilde{\epsilon}_a$ , respectively.

In our case, for each of the three calibrations (short circuit, open-ended and water) three measurements were made; similarly, six measurements at different depths in the agar were performed. Thus, for both the relative permittivity and the electrical conductivity, two values are obtained: the average value on different calibrations (Figure 4.12) and the average value on different calibrations and different depths (Figure 4.13).

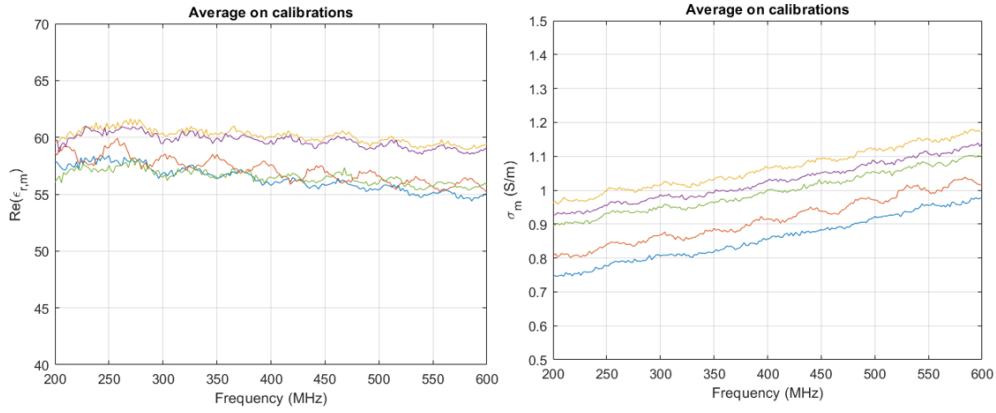


Figure 4.12: Average value on different calibrations.

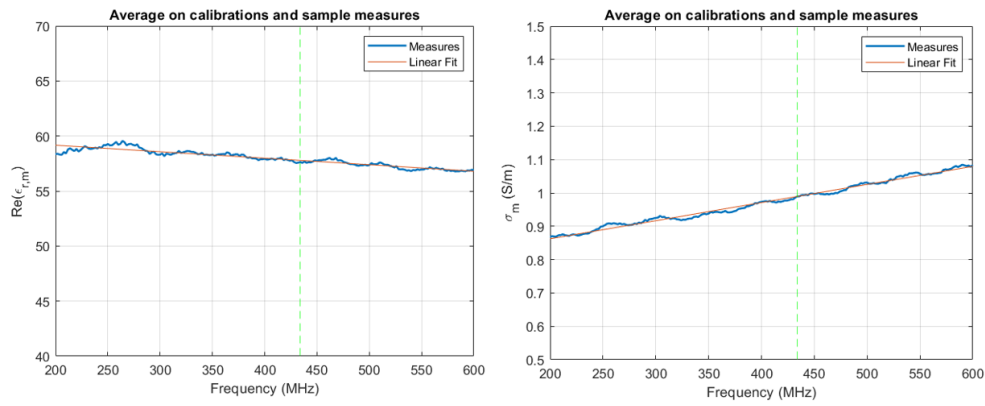


Figure 4.13: Average value on different calibrations and different depths.

These measurements have been performed in three different experimental sessions (so, on three different agar compounds) to obtain a further mean value of agar permittivity and electrical conductivity (Subsection 4.4.2).

In the experimental case, since thermal parameters can not be changed, only electrical ones are modified by varying salt (conductivity  $\sigma$ ) and sugar (permittivity  $\epsilon_r$ ) concentrations. In particular, compared to water, an higher sugar concentration decreases the  $\epsilon_r$ , while an higher salt concentration increases  $\sigma$  of the mixture.

## 4.4.2 Error analysis

As mentioned above, knowing the dielectric characteristics of the medium (in this case, the agar mimicking muscle tissue) is fundamental for a simulation closer to the reality. However, to obtain a “perfect” measure without uncertainties is not possible: the agar mixture will never be exactly the same every time it is prepared and, furthermore, the measuring instrument (the coaxial probe) is affected by uncertainties itself. For these reasons, error analysis of acquired measurements was necessary.

In particular, two methods have been used to measure both  $\epsilon_r$  and  $\sigma$ : method 1 consists of a coaxial probe measurement of the reflection coefficients followed by an appropriate application of the method proposed by Marsland and Evans [51] (Subsection 4.4.1); method 2 consists of direct measure of  $\epsilon_r$  and  $\sigma$  using a SPEAG probe.

Four measurement sessions have been performed (Feb21, Jun21, July21 and Aug21): for each one, a number of repetitions at different depths were done, resulting in several measurements of the same sample under the same conditions (i.e., repeated measurements, useful for limiting random errors).

Being repeated measurements, the average (4.3) is taken as their best value and the standard deviation of the mean (SDM)(4.4) as the error:

$$\bar{x} = \frac{\sum_i x_i}{N}, \quad (4.3)$$

$$SDM = \frac{SD}{\sqrt{N}}, \quad (4.4)$$

where SD is the standard deviation, equal to  $SD = \sqrt{\frac{1}{N-1} \sum_i (x_i - \bar{x})^2}$ ,  $N$  is the number of values, and  $x_i$  is the  $i$ -th value. In this way, for each measurement session three values are obtained for method 1 (Feb21, Jun21 and July21) and three values for method 2 (Jun21, July21 and August21), as reported in tables 4.2 and 4.3.

Method 1			
Session	$\bar{\epsilon}_{r,1}$	$SD$	$SDM$
Feb 21	58.02	2.11	0.64
Jun 21	59.62	3.22	1.14
Jul 21	57.64	1.89	0.85

(a)  $\bar{\epsilon}_{r,1}$  Method 1

Method 2			
Session	$\bar{\epsilon}_{r,2}$	$SD$	$SDM$
Jun 21	59.84	4.59	3.25
Jul 21	58.88	3.16	1.19
Ago 21	57.31	2.35	1.66

(b)  $\bar{\epsilon}_{r,2}$  Method 2

Table 4.2:  $\bar{\epsilon}_r$  measured with two methods.

	Method 1		
Session	$\sigma$ (S/m)	$SD$ (S/m)	$SDM$ (S/m)
Feb 21	0.86	0.08	0.02
Jun 21	1.11	0.14	0.05
Jul 21	0.99	0.08	0.04

(a)  $\sigma$  Method 1

	Method 2		
Session	$\sigma$ (S/m)	$SD$ (S/m)	$SDM$ (S/m)
Jun 21	0.86	0.15	0.11
Jul 21	0.88	0.08	0.03
Ago 21	0.87	0.06	0.04

(b)  $\sigma$  Method 2

Table 4.3:  $\sigma$  measured with two methods.

Therefore, for each method we have 3 estimates of the same quantity ( $\epsilon_r$  and  $\sigma$ ) but under different conditions: a suitable method to combine such measurements (independent measurements) is to perform a weighted average ( $x_{wav}$ ) [52]. In particular, the following relation is applied:

$$x_{wav} = \frac{\sum_i w_i x_i}{\sum_i w_i}, \quad (4.5)$$

where  $w_i$  are the weights, equal to  $w_i = 1/\delta x_i^2$ , in which  $\delta x_i$  is the  $i$ -th standard deviation.

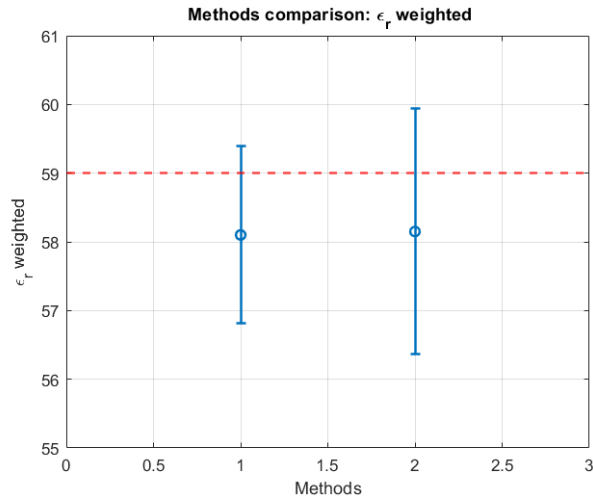
The results obtained by applying equation (4.5), are shown in Table 4.4.

	$\epsilon_r$	$\sigma$ (S/m)
Method 1	$58.10 \pm 1.29$	$0.95 \pm 0.05$
Method 2	$58.15 \pm 1.74$	$0.87 \pm 0.05$

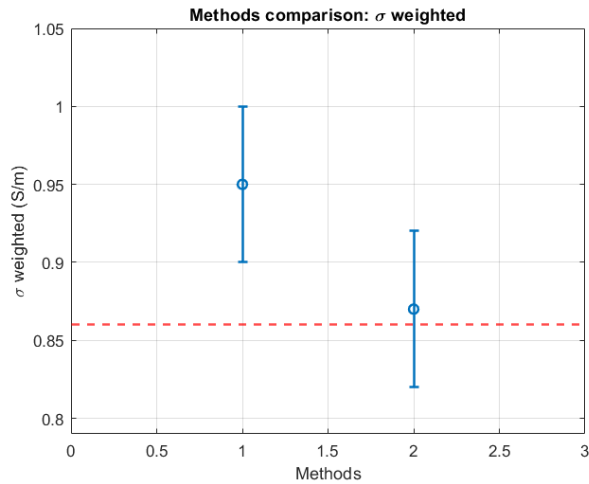
Table 4.4: Weighted dielectric parameters measured.

The values of permittivity and electrical conductivity that we tried to reproduce with the agar-based mixture are those of the muscle tissue at  $f = 434$  MHz, i.e.,  $\epsilon_r = 59$  and  $\sigma = 0.86$  S/m [21].

For  $\epsilon_r$ , the discrepancy between the values obtained with the two different methods is 0.05 (very low, especially compared to their absolute values), smaller than the uncertainties obtained in the two cases (consistent measurements). Moreover, as can be seen in Figure 4.14a, the error bands are overlapped (compatible measurements) and also include the expected value of  $\epsilon_r$ . Hence, for the permittivity the obtained results seem to be reasonable.



(a) Error bars: permittivity  $\epsilon_r$ .



(b) Error bars: conductivity  $\sigma$ .

Figure 4.14: Error analysis results. Red dotted lines indicate expected values.

Considering  $\sigma$  (Figure 4.14b), the obtained discrepancy is 0.08 S/m (almost twice the respective uncertainties): this is due to the value found with method 1 during the second session (Jun21), which resulted in a higher mean sigma value and standard deviation ( $1.11 \pm 0.14$  S/m) than those obtained in the other two measurement sessions. The cause of this marked difference is probably the fact that, in this case, the dielectric parameters have been measured five days after preparing the agar mixture, while in the other cases the measurements were carried out one or two days after agar mixture preparation: during this longer period of time, the mixture dried out more, increasing the salinity.

# Chapter 5

## Conclusions

In this thesis, a complete demonstrator reproducing an apparatus for hyperthermia treatments in the neck region has been implemented. The final aim was to test a SAR-based focusing algorithm with both simulations and experimental measurements. To perform numerical simulations predicting SAR and temperature distribution in the phantom, COMSOL Multiphysics has been used.

The optimized phases found with a PSO algorithm in MATLAB were used to feed a circular array of 8 patch antennas around the neck prototype: overall, the obtained temperature maps have shown that using a single ring of antennas the focusing algorithm works well on the  $xy$ -plane on which the phased array lays, while along the  $z$ -axis (axis of the neck) focusing is more difficult to control.

The characterization of the agar-based mixture (carried out with proper probes) and electronic components (through a VNA) represented an important part of this work.

The system presented in this thesis, can be considered uniform from the dielectric and thermal properties point of view: the target zone (tumor) and the rest of surrounding healthy tissues are indeed mimicked with the same compound of agar, sugar, salt and water (same proportions).

In a future work, since the tumor tissue properties are different from those of healthy tissue (for example, tumor tissues have a lower relative permittivity, but an higher electrical conductivity [53]), the study can be carried out under more realistic conditions, by introducing into the prototype a sphere with different dielectric properties simulating the tumor and, starting from the experimental and simulation setup so far defined, trying to focus the SAR on this target.

Other possible future developments could be: (1) to optimize not only the phases, but also the amplitudes (in the considered thesis, the same constant amplitude has been given in input to each antenna). Due to the higher degrees of freedom, it is probable that by optimizing both phases and amplitudes, the SAR and temperature focusing will be more precise; (2) to simulate the cooling effect of the trachea by inserting a small tube blowing air: in the experimental setup so far implemented, the trachea is modeled with a single opening tube, so the air does not circulate as it does in the trachea; (3) to implement a more sophisticated control system on the electronic setup, in order to avoid unintended malfunctioning of the components (especially the power amplifiers) due to overheating of the elements themselves.

The final goal for the future is to use this demonstrator as a test-bed for the implementation of innovative numerical techniques aimed at improving the temperature monitoring in the heated region during hyperthermia treatments by creating a “library” of temperature maps, where each map corresponds to a random variation of the parameters in Maxwell’s and bioheat equations. In particular, since the numerical simulation are based on experimental model, only dielectric parameters (permittivity and conductivity) will be varied as these are the ones that can be experimentally varied in the phantom.

# Bibliography

- [1] N. Datta et al., “Local hyperthermia combined with radiotherapy and/or chemotherapy: Recent advances and promises for the future,” *Cancer Treat. Rev.*, vol. 41, pp. 742–53, 2015.
- [2] C.S. Cleeland et al., “Reducing the toxicity of cancer therapy: recognizing needs, taking action,” *Nat. Rev. Clin. Oncol.*, vol. 9, pp. 471-8, 2012.
- [3] A. Bakker, J. van der Zee, G. van Tienhoven, H.P Kok, C.R.N. Rasch & H. Crezee, “Temperature and thermal dose during radiotherapy and hyperthermia for recurrent breast cancer are related to clinical outcome and thermal toxicity: a systematic review,” *Int. J. Hyperthermia*, vol. 36, no. 1, pp. 1023-38, 2019.
- [4] M. M. Paulides et al., “The HYPERcollar: A novel applicator for hyperthermia in the head and neck,” *Int. J. Hyperthermia*, vol. 23, no. 7, pp. 567–76, 2007.
- [5] U. Lucia (2017). Elementi di Ingegneria delle Terapie Termiche. CLUT, Torino, pp. 1-131. ISBN 978-88-7992-415-3
- [6] M.M. Paulides, H. Dobsicek Trefna, S. Curto, D.B. Rodrigues, “Recent technological advancements in radiofrequency and microwave-mediated hyperthermia for enhancing drug delivery”, *Adv. Drug Deliv. Rev.*, vol. 163-164, pp. 3-18, 2020.
- [7] N. Cihoric et al., “Hyperthermia-related clinical trials on cancer treatment within the clinicaltrials.gov registry,” *Int. J. Hyperthermia*, vol. 31, no. 6, pp. 609-614, 2015.
- [8] N. R. Datta, S. Rogers, D. Klingbiel, S. Gómez, E. Puric, and S. Bodis, “Hyperthermia and radiotherapy with or without chemotherapy in locally advanced cervical cancer: A systematic review with conventional and network meta analyses,” *Int. J. Hyperthermia*, vol. 32, no. 7, pp. 809-821, 2016.

- [9] R. Colombo, A. Salonia, Z. Leib, M. Pavone-Macaluso, & D. Engelstein, “Long-term outcomes of a randomized controlled trial comparing thermochemotherapy with mitomycin-c alone as adjuvant treatment for non-muscle-invasive bladder cancer”, *BJU Int.*, vol. 107, no. 10, pp. 912–8, 2011.
- [10] K. Sugimachi, H. Kuwano, H. Ide, T. Toge, M. Saku, & Y. Oshiumi, “Chemotherapy combined with or without hyperthermia for patients with oesophageal carcinoma: a prospective randomized trial”, *Int. J. Hyperthermia*, vol. 10, no. 4, pp. 485–93, 1994.
- [11] M. Kroesen et al., “Confirmation of thermal dose as a predictor of local control in cervical carcinoma patients treated with state-of-the-art radiation therapy and hyperthermia,” *Radiother. Oncol.*, vol. 140, pp. 150-158, 2019.
- [12] N. R. Datta, S. Rogers, S. Gómez Ordóñez, E. Puric, & S. Bodis, “Hyperthermia and radiotherapy in the management of head and neck cancers: A systematic review and meta-analysis,” *Int. J. Hyperthermia*, vol. 32, no. 1, pp. 31-40, 2016.
- [13] E. Jones, D. Thrall, M. W. Dewhurst, & Z. Vujaskovic, “Prospective thermal dosimetry: The key to hyperthermia’s future”, *Int. J. Hyperthermia*, vol. 22, pp. 247–53, 2006.
- [14] M. Franckena et al. “Hyperthermia dose–effect relationship in 420 patients with cervical cancer treated with combined radiotherapy and hyperthermia”, *Eur. J. Cancer* vol. 45, pp. 1969–78, 2009.
- [15] Z. Rijnen, J. F. Bakker, R. A. M. Canters, P. Togni, G. M. Verduijn, P. C. Levendag, G. C. van Rhoon, & M. M. Paulides, “Clinical integration of software tool VEDO for adaptive and quantitative application of phased array hyperthermia in the head and neck,” *Int. J. Hyperthermia*, vol. 29, no. 3, pp. 181–93, 2013.
- [16] M. Paulides, Z. Rijnen, J. Bakker, P. Togni, P. Levendag & G. Van Rhoon, “Treatment planning guided RF hyperthermia,” *42nd European Microwave Conference (EuMC)*, pp. 628-31, 2012.
- [17] R. Gaffoglio, M. Righero, G. Giordanengo, M. Zucchi and G. Vecchi, “Fast Optimization of Temperature Focusing in Hyperthermia Treatment of Sub-Superficial Tumors”, *IEEE J. Electromagn. RF Microw. Med. Biol.*, vol. 5, no. 3, pp. 286-93, 2021.

- [18] V. Palma, D. Barba, M. Cortese, M. Martino, S. Renda & E. Meloni, “Microwaves and Heterogeneous Catalysis: A Review on Selected Catalytic Processes,” *Catalysts*, vol. 10, p. 246, 2020.
- [19] E.I. Edeh, “Electromagnetic fields (EMFS) and public health: shaping research agenda in the wake of 5G tech”, *1 st Digital Africa Week*, Abuja, Nigeria, 2019.
- [20] C. Donaghy-Spargor & A. Yakovlev, “Oliver Heaviside’s electromagnetic theory”, *Phil. Trans. R. Soc*, 2018.
- [21] P. A. Hasgall et al., *IT’IS database for thermal and electromagnetic parameters of biological tissues*, 2018. [Online]. Available: <http://www.itis.ethz.ch/database>
- [22] P. Debye, *Polar Molecules*, N.Y.: *Chemical Catalogue Company*, 1929.
- [23] K.S. Cole, R.H. Cole, “Dispersion and absorption in dielectrics: I. Alternating current characteristics,” *J. Chem. Phys.*, pp. 341-51, 1934.
- [24] H. H. Pennes, “Analysis of tissue and arterial blood temperatures in the resting human forearm,” *J. Appl. Physiol.*, vol. 1, no. 2, pp. 93–122, 1948.
- [25] J. van der Zee, M. de Bruijne, J.W.M. Mens et al. “Reirradiation combined with hyperthermia in breast cancer recurrences: overview of experience in Erasmus MC,” *Int. J. Hyperthermia*, vol. 26, pp. 638–48, 2010.
- [26] T. Drizdal, M. M. Paulides, N. van Holthe, and G. C. van Rhoon, “Hyperthermia treatment planning guided applicator selection for subsuperficial head and neck tumors heating,” *Int. J. Hyperthermia*, vol. 34, no. 6, pp. 704–13, 2018.
- [27] IEEE Transactions on Antennas and Propagation, vols. AP-17, No. 3, May 1969; AP-22, No. 1, January 1974; and AP-31, No. 6, Part II, November 1983.
- [28] Constantine A. Balanis. “Antenna Theory: Analysis and Design,” 3rd Edition. Wiley-Interscience, 2016.
- [29] J. D. Jackson, *Classical Electrodynamics*, 3rd ed. Wiley, 1999.
- [30] COMSOL Multiphysics, version 5.6. [www.comsol.it](http://www.comsol.it), 2020.

- [31] J.-M. Jin and D. J. Riley, “Finite Element Analysis of Antennas and Arrays”, John Wiley Sons, Inc., 2009.
- [32] <https://speag.swiss/products/dak/dak-probes/>
- [33] M. M. Paulides, J. F. Bakker, N. Chavannes, and G. C. van Rhoon, “A patch antenna design for application in a phased-array head and neck hyperthermia applicator,” *IEEE Trans. Biomed. Eng.*, vol. 54, no. 11, pp. 2057–63, 2007.
- [34] Hartsgrove, G., Kraszewski, A. & A. Surowiec, “Simulated biological materials for electromagnetic radiation absorption studies”, *Bioelectromagnetics*, vol.8, pp. 29-36, 1987.
- [35] G. G. Bellizzi, T. Drizdal, G. C. van Rhoon, L. Crocco, T. Isernia, and M. M. Paulides, “The potential of constrained SAR focusing for hyperthermia treatment planning: analysis for the head & neck region,” *Phys. Med. Biol.*, vol. 64, no. 1, 2018.
- [36] H. P. Kok, P. M. van Haaren, J. B. van de Kamer, J. Wiersma, J. D. van Dijk, and J. Crezee, “High-resolution temperature-based optimization for hyperthermia treatment planning,” *Phys. Med. Biol.*, vol. 50, no. 13, pp. 3127–41, 2005.
- [37] J. Kennedy and R. Eberhart, “Particle swarm optimization,” *Proceedings of ICNN’95 - International Conference on Neural Networks*, vol.4, pp. 1942-48, 1995.
- [38] ICNIRP Guidelines for limiting exposure to electromagnetic fields (100 KHZ TO 300 GHZ) published in health phys, vol. 118, no.5, pp. 483–524, 2020.
- [39] G.C. van Rhoon & P. Wust, “Introduction: Non-invasive thermometry for thermotherapy,” *Int. J. Hyperthermia*, vol. 21, no. 6, 2005.
- [40] L. Pasquato, “Sistema per la misura di temperatura con sensori in fibra ottica per l’acceleratore di ioni negativi dell’esperienza MITICA”, Master thesis, Università degli studi di Padova, Italia, 2015.
- [41] | Thair B. A. et al., “Fabrication of fiber grating by phase mask and its sensing application,” *J. Optoelectron. Adv. Mater.*, vol 8, pp. 1604-1609, 2006.

- [42] Y. Wang, X. Liu, M. Zhang, X. Bai & B. Mou, "Fiber Bragg Grating Sensors for Pile Jacking Monitoring in Clay Soil," *Sensors*, vol. 20, no. 18, 2020.
- [43] Y. J. Rao, "Optical in-fiber Bragg grating sensor systems for medical applications," *J. Biomed. Opt.*, vol. 3, no. 1, p. 38, 1998.
- [44] D. Lo Presti et al., "Fiber Bragg Gratings for Medical Applications and Future Challenges: A Review," *IEEE Access*, vol. 8, pp. 156863-156888, 2020.
- [45] M. Riedl, "Optical Design Fundamentals for Infrared Systems", Second Edition, SPIE Press, Bellingham, WA, 2001.
- [46] H. Loisel, C. Jamet & J. Riedi, "Remote Sensing", *Geophys. Monogr. Ser.*, 2009.
- [47] W. Wien, "On the division of energy in the emission-spectrum of a black body," *Lond. Edinb. Dublin Philos. Mag. J. Sci.*, Series 5, vol. 43, no. 262, pp. 214–20, 1897.
- [48] Determination of thermal conductivity and thermal diffusivity - Part 2: Transient plane heat source (hot disc) method (ISO 22007-2:2008)
- [49] A. La Gioia, E. Porter, S. Salahuddin, M. O'halloran, "Impact of radial heterogeneities of biological tissues on dielectric measurements," *International Conference on Electromagnetics in Advanced Applications (ICEAA)*, 2017.
- [50] A. La Gioia et al., "Open-Ended Coaxial Probe Technique for Dielectric Measurement of Biological Tissues: Challenges and Common Practices," *Diagnostics (Basel)*, vol. 8, no. (2), p. 40, 2018.
- [51] T. Marsland, S. Evans, "Dielectric measurements with an openended coaxial probe," *IEE Proc.* , vol. 134, no. 4, pp. 341-3490, 1987.
- [52] J. Taylor, "Introduction to Error Analysis, the Study of Uncertainties in Physical Measurements," 2nd Edition, Published by University Science Books, 648 Broadway, Suite 902, New York, NY 10012, 1997.
- [53] Y. Cheng, M. Fu, "Dielectric properties for non-invasive detection of normal, benign, and malignant breast tissues using microwave theories," *Thorac Cancer*, vol.9(4), pp. 459-465, 2018.